Received: 30 May 2022 | Revised: 8 March 2023 | Accepted: 12 March 2023

DOI: 10.1002/nme.7241

RESEARCH ARTICLE

WILEY

Time-continuous and time-discontinuous space-time finite elements for advection-diffusion problems

Max von Danwitz[1] | **Igor Voulis**[2] | **Norbert Hosters**[3] | **Marek Behr**[3]

[1]Institute for Mathematics and Computer-Based Simulation (IMCS), University of the Bundeswehr Munich, Neubiberg, Germany

[2]Institute for Numerical and Applied Mathematics, University of Göttingen, Göttingen, Germany

[3]Chair for Computational Analysis of Technical Systems (CATS), RWTH Aachen University, Aachen, Germany

Correspondence
Max von Danwitz, Institute for Mathematics and Computer-Based Simulation (IMCS), University of the Bundeswehr Munich, Werner-Heisenberg-Weg 39, D-85577 Neubiberg, Germany.
Email: max.danwitz@unibw.de

Funding information
dtec.bw – Digitalization and Technology Research Center of the Bundeswehr. dtec.bw is funded by the European Union – NextGenerationEU; University of the Bundeswehr Munich

Abstract

We construct four variants of space-time finite element discretizations based on linear tensor-product and simplex-type finite elements. The resulting discretizations are continuous in space, and continuous or discontinuous in time. In a first test run, all four methods are applied to a linear scalar advection-diffusion model problem. Then, the convergence properties of the time-discontinuous space-time finite element discretizations are studied in numerical experiments. Advection velocity and diffusion coefficient are varied, such that the parabolic case of pure diffusion (heat equation), as well as, the hyperbolic case of pure advection (transport equation) are included in the study. For each model parameter set, the L_2 error at the final time is computed for spatial and temporal element lengths ranging over several orders of magnitude to allow for an individual evaluation of the methods' spatial, temporal, and space-time accuracy. In the parabolic case, particular attention is paid to the influence of time-dependent boundary conditions. Key findings include a spatial accuracy of second order and a temporal accuracy between second and third order. The temporal accuracy tends toward third order depending on how advection-dominated the test case is, on the choice of the specific discretization method, and on the time-(in)dependence and treatment of the boundary conditions. Additionally, the potential of time-continuous simplex space-time finite elements for heat flux computations is demonstrated with a piston ring pack test case and a subtractive manufacturing test case.

KEYWORDS

advection-diffusion problems, simplex space-time, space-time finite elements, stabilized finite element methods

1 | INTRODUCTION

1.1 | Motivation

Multiple features make space-time finite elements an attractive solution strategy for time-dependent partial differential equations (PDE). First, space-time finite elements provide a uniform framework for error analysis as no distinction is made between spatial and temporal coordinates,[1] which can also be used in adaptive refinement of the combined

space-time mesh.[2] Moreover, space-time finite elements allow for parallel-in-time computations which have inherently more potential for parallelization than spatial finite elements combined with a sequential time-stepping scheme.[3] Furthermore, space-time finite elements are a natural choice to discretize time-dependent spatial computational domains, for example, in fluid–structure interaction simulations.[4-7] In particular, simplex space-time finite elements[8] can provide a boundary conforming space-time mesh for spatial domains that change topology over time.[9]

To benefit from these advantages, space-time finite elements have been used to perform simulations in various fields of computational fluid dynamics (CFD). Recent examples of simplex space-time simulations include the computation of complex fluid flows in production engineering applications[10,11] and the computation of dense granular flows.[12] Likewise, compressible flows have been successfully simulated on unstructured space-time meshes.[13-15] Note that the solution of transient three-dimensional problems with space-time finite elements requires four-dimensional meshes. Recent advances in generation,[9,16,17] adaptation,[18] and numerical handling[19,20] of four-dimensional meshes mark the state-of-the-art in this active research field.

For efficiency considerations and refinement strategies, it is important to know the convergence behavior of the space-time finite element solution toward the physical or analytical solution of the simulated test case. However, for simulations based on the incompressible or compressible Naiver–Stokes equations it is an intricate task to estimate exact convergence orders, since numerical reference solutions can be influenced by round-off errors or implementation issues. Instead, we consider in this paper advection-diffusion problems—which lend themselves to an analytical solution—as a prototype for more complex flow problems.[21] Based on the advection-diffusion equation, one can investigate the performance of numerical schemes with respect to transient, advective, and diffusive effects as well as their interplay. Besides, advection-diffusion equations also model a variety of physical problems, for example, the concentration of a chemical species transported by an ambient flow or the temperature of a fluid streaming along a heated wall.[21] Therefore, it is of great interest to analyze the convergence behavior of numerical schemes for advection-diffusion problems.

1.2 | Literature review

Shakib and Hughes[22] present a Fourier analysis of space-finite elements with tensor-product structure applied to an advective-diffusive model problem with periodic boundary conditions. The method is found to be third-order accurate with respect to the time step size for the pure advection and pure diffusion case. A summary of space-time finite element methods for convective transport problems is provided by Donea and Huerta along with numerical tests.[23]

Moreover, linear tensor-product space-time finite elements can be related to a spatial discretization with finite elements and a temporal discretization with the Crank–Nicolson scheme.[8] Studies of this resulting method often focus either on parabolic problems (heat equation)[24] or on the pure advection case (transport equation).[25] Moreover, a Crank–Nicolson type space-time finite element method for evolution problems on moving meshes is proposed and analyzed by Hansbo.[26] The method uses tensor product elements that are inclined in space-time with a slope given by the convection velocity. It is reported that the aligned space-time orientation improves the precision and facilitates the solution of the discrete system.

Focusing on the parabolic limit case, time-continuous tensor-product space-time finite elements have been analyzed by Aziz and Monk.[27] In more recent works, also unstructured space-time finite elements which do not require any tensor-product structure are addressed, for example, by Steinbach.[28] Furthermore, Langer and Schafelner[2,29] investigate the scaling behavior of unstructured space-time finite element methods for parabolic problems in parallel computations. Note that this work is also extended to hexahedral space-time discretizations.[30] Moreover, Langer and Zank propose and investigate new efficient direct solvers for time-continuous tensor-product discretizations of the parabolic initial boundary value problem.[31] The influence of linear constraints, for example, time-dependent Dirichlet boundary conditions, on discontinuous Galerkin time discretization methods for parabolic problems is treated by Voulis and Reusken.[32]

1.3 | Scientific novelty and limitations

To the best of the authors' knowledge, there is no previous comprehensive numerical study that analyzes the convergence behavior of tensor-product and simplex-type finite elements for the complete range of model parameters of advection-diffusion problems and for spatial and temporal element sizes over several orders of magnitude. On the one hand, the computational evaluation of the convergence behavior is advantageous in the sense that a simple variation of the input parameters allows to switch from a parabolic to a hyperbolic problem. Therefore, the computational approach

facilitates a study of the precise influence of parameter variations. On the other hand, the numerical study is limited to specific test cases and for those considers only the L_2 norm and a nodal measure of the error at the final time. Still, it is expected that the results also hold for other test cases of similar nature.

1.4 | Paper organization

In the remainder, we proceed as follows. In Section 2, four space-time discretizations are presented and descriptive naming is proposed. In Section 3, we apply the methods to an initial boundary value problem based on the advection-diffusion equation. Section 4 collects the results of a computational error analysis of the time-discontinuous discretizations and compares the results with the theoretically expected convergence behavior. In Section 5, we demonstrate the particular potential of simulations on time-continuous simplex space-time meshes in a piston ring pack and subtractive manufacturing application. Concluding remarks are offered in Section 6.

2 | METHOD CLASSIFICATION

To introduce the specific space-time discretizations investigated in this work, the naming of involved entities is briefly reviewed.[1,15] We consider a spatial computational domain $\Omega \subset \mathbb{R}^{n_{\text{sd}}}$, where n_{sd} denotes the number of spatial dimensions. That domain Ω and a time interval, $I = [0, t_f] \subset \mathbb{R}$, span the space-time continuum $Q \subset \mathbb{R}^{n_{\text{sd}}+1}$. In the following, we consider four ways to approximate the solution of PDEs on Q with finite elements. Sample slicings Q^h of the space-time domain $Q = [x_0, x_3] \times [t_0, t_3]$ are shown in Figure 1. The first two discretization techniques (Figure 1A,B) seek an approximation that is continuous across Q. In contrast, the second two (Figure 1C,D) seek an approximation that is discontinuous at certain times, which leads to a discontinuous Galerkin method for the temporal discretization. In these time-discontinuous cases, Q is sliced into space-time slabs $Q_n = (t_n, t_{n+1}) \times \Omega$. As indicated in the drawings of Figure 1C,D, the boundary of each space-time discretization consists of three parts: the spatial discretization at the lower time level $\Omega_{\text{l}}^h = \Omega^h(t = t_n)$, the spatial discretization at the upper time level $\Omega_{\text{u}}^h = \Omega^h(t = t_{n+1})$, and the discretization of the space-time boundary $P \subset \mathbb{R}^{n_{\text{sd}}}$ which is the temporal evolution of the spatial domain boundary $\Gamma \subset \mathbb{R}^{n_{\text{sd}}-1}$. The size of space-time slabs in temporal direction is denoted by Δt. To later apply one uniform finite element formulation for the time-continuous and time-discontinuous cases, we regard the complete space-time domain Q in the time-continuous case as space-time slab Q_0.

Both time-discretization approaches can be combined with prismatic elements with tensor-product structure, or simplex elements. The combinations form the four discretization methods C-PST, C-SST, D-PST, and D-SST. In PST methods, a discretization of Q_n with prismatic space-time elements can be easily obtained by extrusion of a spatial discretization of Ω in time. C-PST is a continuous finite element discretization in space and time as described by Aziz and Monk.[27] When combined with linear shape functions, it is also known as cg(1)cg(1). The time-discontinuous D-PST method is also referred to as cg(1)dg(1), for example, by Quarteroni et al.[33] SST discretizations can be generated by subdividing the prismatic elements into simplex elements Q_n^e (Figure 1B,D). More complex SST mesh generation procedures also allow for local temporal refinement by node insertion[8] or fully unstructured space-time meshes[15] as shown in Figure 2.

For each space-time slab Q_n, an H^1-conformal finite element approximation space $H_{h,n}^1$ is constructed based on (space-time) element-wise defined basis functions.[15] In the subsequent numerical examples, we employ finite elements of degree 1. Following the notation of Ern and Guermand,[34] we consider the $\mathbb{PR}_1$ and $\mathbb{Q}_1$ basis functions of the simplex-based prismatic and cuboid Lagrange finite elements in case of PST discretizations. In case of SST discretizations, we use the $\mathbb{P}_1$ basis functions of the simplical Lagrange finite element, which is a triangle for two-dimensional domains (one-dimensional [1D] plus time, e.g., Section 4), a tetrahedron for three-dimensional domains (2D plus time, e.g., Section 5.1) and a pentatope for four-dimensional domains (3D plus time, e.g., Section 5.2). The four space-time discretizations introduced, are now employed in the solution of advection-diffusion problems.

3 | APPLICATION TO ADVECTION-DIFFUSION EQUATION

We consider the time-dependent linear advection-diffusion equation

$$\text{res}(u) := \frac{\partial u}{\partial t} + \mathbf{a} \cdot \nabla u - k\, \Delta u = 0. \tag{1}$$

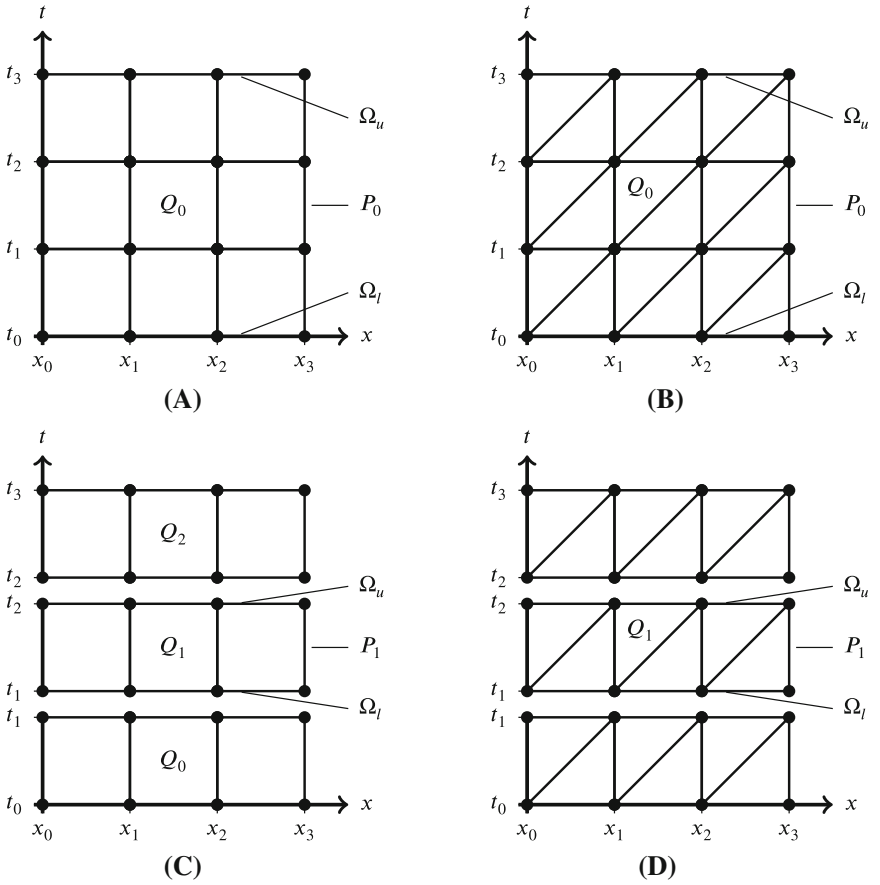

FIGURE 1 Space-time discretization methods. (A) Time-continuous prismatic space-time method (C-PST); (B) Time-continuous simplex space-time method (C-SST); (C) Time-discontinuous prismatic space-time method (D-PST); (D) Time-discontinuous simplex space-time method (D-SST).

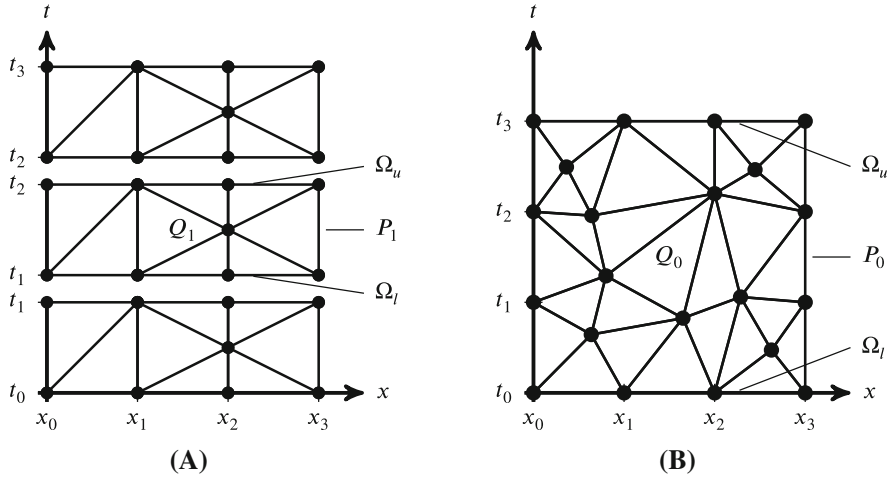

FIGURE 2 Variants of simplex space-time discretization methods. (A) Local temporal refinement in D-SST mesh; (B) Fully unstructured C-SST mesh.

Therein, the scalar unknown, $u(\mathbf{x}, t)$ is a function of the spatial coordinates ($\mathbf{x} = (x, y, z)^T$ for $n_{\text{sd}} = 3$) and time. The advection velocity is a given vector $\mathbf{a}$, and the constant diffusion coefficient is denoted by k. As usual, the Laplacian of u abbreviates $\Delta u = \nabla \cdot \nabla u$, based on the spatial gradient ∇u. Advection velocity and diffusion coefficient can be varied, such that the parabolic case of pure diffusion ($\mathbf{a} = \mathbf{0}$), as well as the hyperbolic case of pure advection ($k = 0$) are included. In the former case, Equation (1) is the heat equation, in the latter case the transport equation. Furthermore, the above equation lends itself to an analytic solution, hence, facilitating a computational error analysis as presented in Section 4.

A general characterization of advection-diffusion problems can be achieved with the dimensionless Péclet number

$$\text{Pe} := L_c \frac{a}{k}. \tag{2}$$

Therein, a scalar measure of the advection speed, $a = \|\mathbf{a}\|$, is related to the diffusion coefficient k and scaled by a characteristic length L_c. As the dimensionless number compares the importance of advective and diffusive effects for a given test case, one can typically expect solutions with smaller gradients for test cases with lower Péclet number (when diffusion dominates).

To construct an initial boundary value problem, let us consider again a computational domain Q as for example shown in Figure 2B. The associated space-time boundary P is assumed to consist of a Dirichlet part P^D and a Neumann part P^N, such that $P = P^D \cup P^N$ and $P^D \cap P^N = \emptyset$. Then, we obtain an initial boundary value problem, as we require Equation (1) to hold on Q, along with a known initial condition u_0 and given Dirichlet boundary conditions g. Initial and Dirichlet boundary data are assumed to be compatible, namely we require $g(x, t = 0) = u_0(x)$ on the intersection $\Omega(t = 0) \cap P^D$. Furthermore, let $\frac{\partial u}{\partial n}$ denote the derivative of u in the direction of the outwards-pointing boundary normal. Throughout this work, we shall consider homogeneous Neumann boundary conditions, such that the complete statement of the initial boundary value problem reads

$$\text{IBVP} \quad \begin{cases} \text{res}(u(\mathbf{x}, t)) = 0, & \text{on } Q, \\ u(\mathbf{x}, t) = u_0(\mathbf{x}), & \text{at } t = 0, \\ u(\mathbf{x}, t) = g(\mathbf{x}, t), & \text{on } P^D, \\ \frac{\partial u(\mathbf{x}, t)}{\partial n} = 0, & \text{on } P^N. \end{cases} \tag{3}$$

When applying one of the discretization techniques described in Section 2 to Q, the initial condition is enforced on Ω_l of the space-time slab Q_0. The part of a space-time slab Q_n, where Dirichlet boundary conditions are prescribed is denoted by P_n^D. A suitable interpolation of the Dirichlet boundary data g^h (further discussed in Section 4.1) allows us to define the trial function space

$$\mathcal{S}_{h,n} = \left\{ u^h \in H^1_{h,n} \middle| u^h = g^h \text{ on } P_n^D \right\}, \tag{4}$$

and the test function space

$$\mathcal{V}_{h,n} = \left\{ w^h \in H^1_{h,n} \middle| w^h = 0 \text{ on } P_n^D \right\}. \tag{5}$$

Considering that for time-discontinuous discretization methods the finite element approximation is discontinuous at the space-time slab boundaries Ω_l and Ω_u, let $\left(u^h\right)_n^{\pm}$ abbreviate $\lim_{\varepsilon \to 0} u^h(t_n \pm \varepsilon)$.

Using these definitions, a discretized weak form of the initial boundary value problem can be stated as follows: For given initial conditions $\left(u^h\right)_0^- = u_0^h$, find $u^h \in \mathcal{S}_{h,n}$ such that on each time slab Q_n and for all $w^h \in \mathcal{V}_{h,n}$

$$\begin{aligned} 0 = & \int_{Q_n} w^h \cdot \left(\frac{\partial u^h}{\partial t} + \mathbf{a} \cdot \nabla u^h \right) dQ \\ & + \int_{Q_n} \nabla w^h \cdot \left(k \nabla u^h \right) dQ \\ & + \int_{\Omega_l} \left(w^h\right)_n^+ \cdot \left[\left(u^h\right)_n^+ - \left(u^h\right)_n^- \right] d\Omega \\ & + \int_{Q_n} \left(\frac{\partial w^h}{\partial t} + \mathbf{a} \cdot \nabla w^h \right) \cdot \tau_{\text{SUPG}} \cdot \text{res}^h \left(u^h\right) dQ. \end{aligned} \tag{6}$$

In the weak form above, the diffusion term was modified using integration by parts. The resulting boundary integral vanishes, since the test functions vanish on P_n^D and homogeneous Neumann boundary conditions are assumed on P_n^N. Moreover, the initial condition as well as the continuity of u^h between time slabs is weakly enforced with the integral over the spatial computational domain Ω_l, the so-called jump term. Stability of the formulation is achieved with a SUPG term in the fourth integral.[35] We define the stabilization parameter τ_{SUPG} as

$$\tau_{\text{SUPG}} = \left(\begin{bmatrix} \mathbf{a} \\ 1 \end{bmatrix} \cdot \mathbf{G} \begin{bmatrix} \mathbf{a} \\ 1 \end{bmatrix} + \left(C_{\text{inv}} \frac{k}{h_s^2} \right)^2 \right)^{-\frac{1}{2}}, \tag{7}$$

which accounts for local characteristics of the initial boundary value problem. Information about the element's size is included through the space-time element metric tensor $\mathbf{G}$ and a measure for the spatial element length h_s (defined below).

In the definition of τ_{SUPG} (Equation 7), the metric tensor,

$$\mathbf{G} = \left(\frac{\partial(\boldsymbol{\xi}, \tau)}{\partial(\mathbf{x}, t)} \right)^T \mathbf{M} \left(\frac{\partial(\boldsymbol{\xi}, \tau)}{\partial(\mathbf{x}, t)} \right), \tag{8}$$

is based on the inverse of the Jacobian associated with the mapping from reference coordinates, $(\boldsymbol{\xi}, \tau)$, to physical coordinates, $(\mathbf{x}, t)$. Please, note that $\mathbf{G}$ includes spatial and temporal element length scales. For PST discretizations, the temporal element length corresponds to the time step size and $\left(\frac{\partial \tau}{\partial t} \right)^2 = \frac{4}{\Delta t^2}$ recovers the time step contribution to the stabilization parameter definition of the variational multiscale method for incompressible flows.[36,37] The implicit definition of the element length with $\mathbf{G}$ has been tested for anisotropic meshes with elements with large aspect-ratios in the setting of compressible and incompressible flow simulations.[15,37] Moreover, the metric tensor includes a square matrix $\mathbf{M}$ of size $n_{\text{sd}} + 1$, which accounts for the mapping to a regular reference element counteracting the influence of the element's node numbering.[15] A further analysis of node-numbering invariant element length measures for simplex elements is presented by Takizawa et al.[19] Explicit forms of $\mathbf{M}$ for simplex elements read for $d = 2, 3, 4$, respectively,

$$\mathbf{M}_{d=2} = \frac{1}{\sqrt{3}} \begin{pmatrix} 2 & 1 \\ 1 & 2 \end{pmatrix}, \quad \mathbf{M}_{d=3} = \frac{1}{\sqrt[3]{4}} \begin{pmatrix} 2 & 1 & 1 \\ 1 & 2 & 1 \\ 1 & 1 & 2 \end{pmatrix}, \quad \mathbf{M}_{d=4} = \frac{1}{\sqrt[4]{5}} \begin{pmatrix} 2 & 1 & 1 & 1 \\ 1 & 2 & 1 & 1 \\ 1 & 1 & 2 & 1 \\ 1 & 1 & 1 & 2 \end{pmatrix}. \tag{9}$$

For other element types, an appropriate matrix $\mathbf{M}$ is substituted. Recalling that $\mathbf{M}$ accounts for the mapping to a regular reference element, it is clear that discretizations with pure tensor-product reference elements ($\mathbb{Q}_1$) do not need an additional mapping—as the reference element is already regular. Therefore, $\mathbf{M}$ can simply be replaced by the identity matrix. In case of a simplex-based prismatic reference element ($\mathbb{PR}_1$), the partial tensor-product structure of the reference element is reflected in the choice of $\mathbf{M}$ as shown below

$$\mathbf{M} = \begin{cases} \mathbf{M}_{d=n_{\text{sd}}+1} & \mathbb{P}_1 \\ \mathbf{I} & \mathbb{Q}_1 \\ \begin{pmatrix} \mathbf{M}_{d=n_{\text{sd}}} & \mathbf{0} \\ \mathbf{0}^T & 1 \end{pmatrix} & \mathbb{PR}_1. \end{cases} \tag{10}$$

In the second term of Equation (7), the diffusive contribution to τ_{SUPG} requires a measure of the spatial element length h_s. For all considered element types, the length h_s is obtained from the spatial part of the metric tensor $\mathbf{G}_s = [\mathbf{G}]_{n_{\text{sd}} \times n_{\text{sd}}}$ as

$$\frac{1}{h_s^2} = \sqrt{\mathbf{G}_s : \mathbf{G}_s}, \tag{11}$$

where the colon operator denotes the double contraction $\mathbf{G} : \mathbf{G} = \sum_{i,j} G_{ij} \cdot G_{ij}$. Moreover, the constant C_{inv} scales the diffusive contribution to τ_{SUPG}. Inspired by an inverse estimate inequality proven in Reference 38, we chose for $\mathbb{P}_1$ and

$\mathbb{PR}_1$ discretizations

$$C_{\text{inv}} = (n_{\text{sd}} + 1)^2(n_{\text{sd}} + 2) = \begin{cases} 12 & n_{\text{sd}} = 1, \\ 36 & n_{\text{sd}} = 2, \\ 80 & n_{\text{sd}} = 3. \end{cases} \tag{12}$$

For $\mathbb{Q}_1$ discretizations, we use $C_{\text{inv}} \approx 1$. The residual $\text{res}^h(u^h)$ in the SUPG term (the fourth integral in Equation (6)) is based on a least-squares recovery technique for the second-order derivatives to improve the consistency of our formulation in combination with linear finite elements.[39]

For the parabolic case ($\mathbf{a} = \mathbf{0}$) and linear approximation functions, the weak form in Equation (6) is very close to the locally stabilized space-time finite element method presented by Langer and Schafelner in section 3 of Reference 29. Only the definition of the stabilization parameter, τ_{SUPG} or Θ_K, see remark 13.4 of Reference 2, and the enforcement of the initial condition differ. Moreover, we observe that the discretization (Equation 6) is very similar to the Crank–Nicolson scheme. For further remarks on the relationship to the time-stepping scheme, we refer to Reference 8.

To provide a first test case for the four space-time discretization methods, we analyze the transient 1D model problem

$$\text{IBVP 1} \quad \begin{cases} \text{res}(u(x,t)) = 0, & x \in]-1,1[, \quad t \in]0,2], \\ u(x,t) = -\sin(\pi x), & \text{at } t = 0, \\ u(-1,t) = u(1,t), & \text{on } P^D. \end{cases} \tag{13}$$

We consider a time interval $I =]0, 2]$ and the spatial computational domain Ω ($n_{\text{sd}} = 1$) spans from -1 to 1. The model problem is characterized by the periodic boundary conditions and has the analytical solution

$$u(x,t) = -\sin(\pi(x - at))e^{-k\pi^2 t}. \tag{14}$$

The test case setup of IBVP 1 is also discussed by Mojtabi and Deville[40] and on a shifted computational domain by Shakib and Hughes.[22]

In the numerical solution procedure, we discretize the computational domain Q with eight elements in spatial and temporal direction as shown in Figure 3. Due to the periodic boundary conditions $u(-1,t) = u(1,t)$, this leads to eight independent degrees of freedom in spatial direction. As the initial condition is enforced weakly, the time-continuous discretizations have nine nodes in time direction with one degree of freedom each. Therefore, C-PST and C-SST simulations use $9 \times 8 = 72$ degrees of freedom in total in this specific test case. The time-discontinuous methods have two degrees of freedom per time step to approximate the solution in temporal direction, so $16 \times 8 = 128$ degrees of freedom in total for this specific computation.

An advection speed of $a = 1$ and a diffusion coefficient $k = 0.1$ lead to the damped traveling sine wave shown in Figure 3. To quantify the importance of advective and diffusive effects, the purely advective solution, $u_a = u(x,t;k=0)$, and purely diffusive solution, $u_d = u(x,t;a=0)$, are compared to the advection-diffusion solution $u(x,t;a=1,k=0.1)$ (Equation 14). Numerical evaluation of the differences in L_2 norm (over the space-time domain), $\|u - u_a\| \approx 0.844 \cong \|u - u_d\| \approx 0.867$, shows that advective and diffusive effects are of similar importance for this choice of parameter values. We therefore calibrate the Péclet number (Equation 2) for this model problem with a characteristic length $L_c = 1/10$ to obtain $\text{Pe} = 1$ for $a = 1$ and $k = 0.1$.

Comparing the solution of D-PST in Figure 3C with the C-PST solution in Figure 3A, one can note jumps in the solution at the interfaces between the space-time slabs. These small discontinuities in the solution are in line with the weak enforcement of the continuity requirement in the weak form (Equation 6). Also the D-SST solution is discontinuous at the interfaces between space-time slabs. However, these jumps are less pronounced and not visible in the rendering of Figure 3D. Regarding the SST discretizations (in Figure 3B,D), we can note that the solution u is advected along the diagonal edges of the SST discretizations. In this particular case with $\Delta x = \Delta t$ and $a = 1$, the characteristics perfectly align with the finite element edges.

Figure 4 compares the numerical solutions u^h of the four space-time discretization methods to the analytical solution u at the final time t_f. In the plot of the differences $u - u^h$ (Figure 4A), the interpolation error between the nodal values is very prominent. Please, note that this error is inherent to the linear interpolation of a trigonometric function. Removing this unavoidable error (for linear approximation functions), Figure 4B connects the values at the finite element nodes

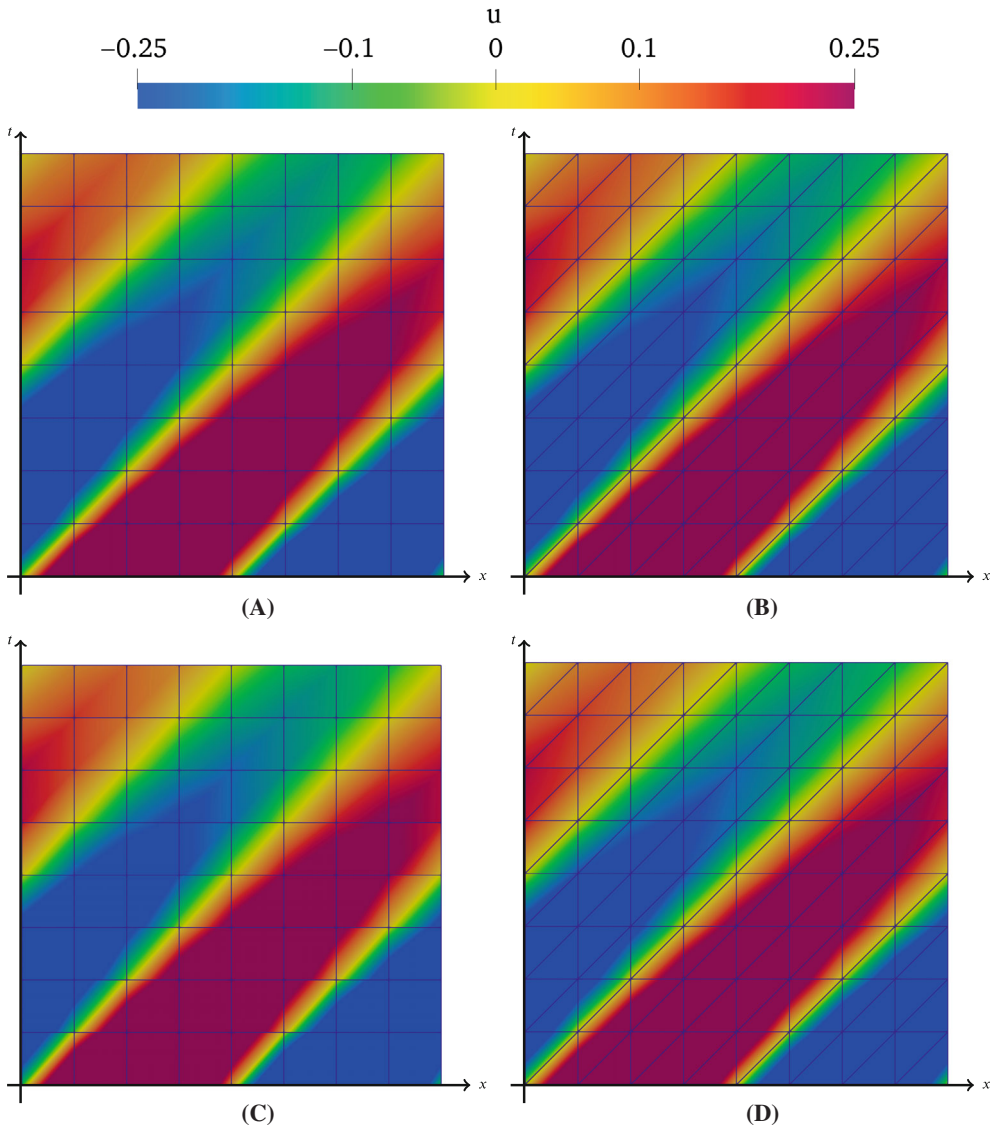

FIGURE 3 Solution of IBVP 1 computed with four space-time discretization methods. (A) C-PST; (B) C-SST; (C) D-PST; (D) D-SST.

with straight line segments. For the employed, very coarse discretizations, the nodal differences of the SST solutions to the analytical solution are smaller, despite the smaller number of degrees of freedom in comparison to the PST methods. Additionally, the D-SST method shows hardly any phase error. Comparing Figure 4A and B, one can observe that the error of the finite element solution at the nodes is of the same order as the interpolation error.

The simulation is repeated on finer meshes with $2^6 = 64$ elements in space and time (medium) and $2^9 = 512$ elements (fine), respectively. Figure 5 shows the differences to the analytical solution at the nodes of the two finer meshes. Clearly, the numerical solution approaches the analytical solution as the mesh is refined. The scales of the nodal differences in Figure 5A,B hint at a second-order convergence of the maximum error for all four methods for uniform space-time refinement. More rigorous convergence studies are carried out for D-PST and D-SST discretizations in the following Section 4. In summary, we conclude that all four space-time discretization schemes can be applied to advection-diffusion problems.

The C-PST method has been analyzed for the heat equation theoretically and with numerical experiments by Aziz and Monk.[27] It is found that the use of linear finite element approximation functions in C-PST leads to a version of the Crank–Nicolson method. Moreover, the tensor-product approach of C-PST leads to a global linear equation system with specific structure for parabolic initial boundary value problems. This structure can be exploited in the construction of an efficient parallel solver as shown by Langer and Zank.[31] Still, we will not further consider the scheme in this paper.

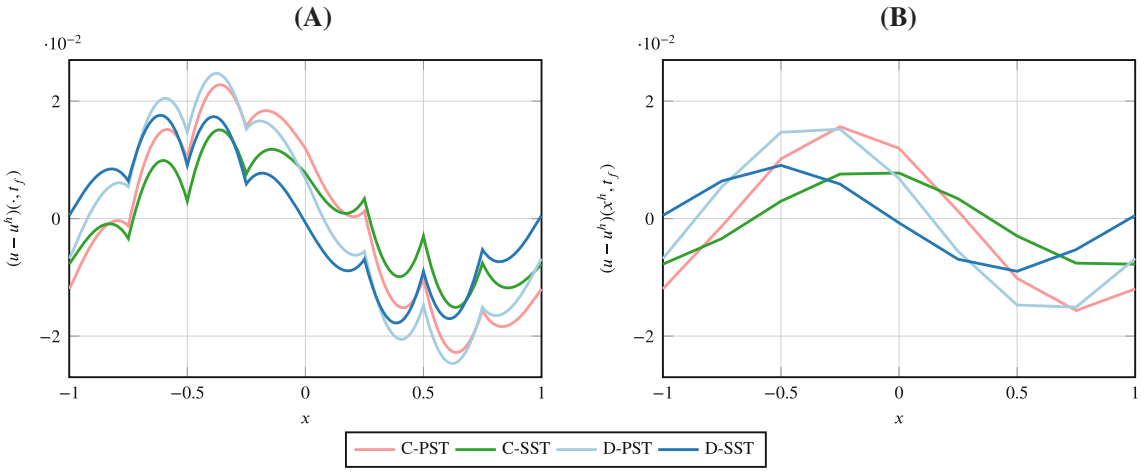

FIGURE 4 Comparison of four space-time methods for IBVP 1 on a coarse mesh. (A) Differences between u and u^h; (B) Differences at nodes x^h.

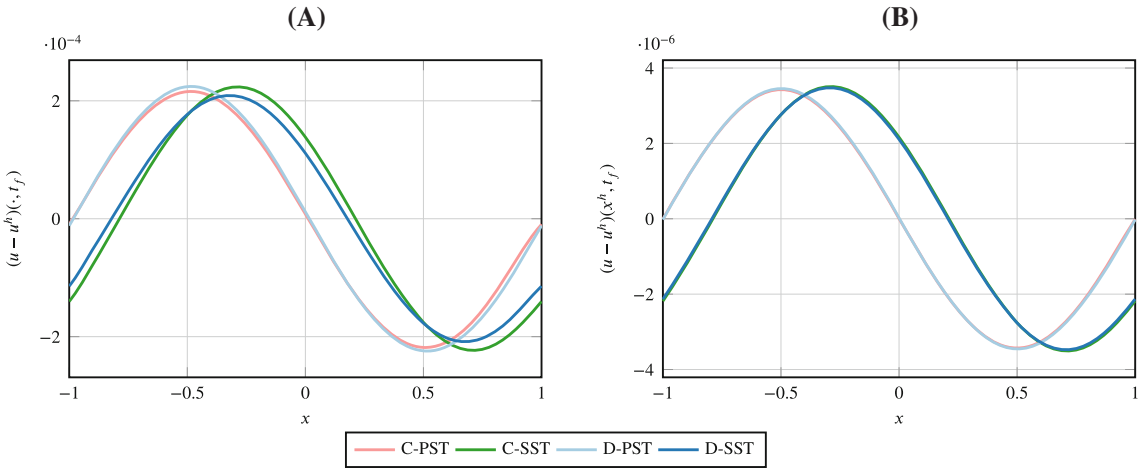

FIGURE 5 Comparison of four space-time methods for IBVP 1 on medium and fine mesh. (A) Differences at nodes x^h of medium mesh; (B) Differences at nodes x^h of fine mesh.

The C-SST method allows for space-time adaptivity on unstructured meshes[29] and in Section 5 the C-SST method is used to include topology changes of the spatial computational domain Ω in a boundary-conforming space-time mesh. However, Section 4 focuses on the time-discontinuous methods, D-PST and D-SST.

4 | COMPUTATIONAL ERROR ANALYSIS OF TIME-DISCONTINUOUS DISCRETIZATIONS

To investigate the convergence of the time-discontinuous space-time discretizations D-PST and D-SST, a computational error analysis is performed. The following space-time convergence studies consider two test cases. Before investigating IBVP 1 (Equation 13) for six model parameter sets in Section 4.2, we first consider the parabolic case ($a = 0$) of a second initial boundary value problem IBVP 2 with time-dependent Dirichlet boundary conditions in Section 4.1. Both initial boundary value problems have analytical solutions, which serve particularly well as reference solutions in the convergence studies, since they are independent of implementation issues or round-off errors introduced in computer arithmetic.

For each model problem, parameter set, and discretization method (D-PST, D-SST) a space-time convergence study with 198 simulations is performed. The numerical simulation settings are obtained as follows. We divide the

computational domain in time direction (up to the final time $t_f = 2$) into n_{ts} space-time slabs of constant size $\Delta t = t_f / n_{\text{ts}}$. We consider 15 levels of recursive temporal refinement such that n_{ts} is doubled from the coarser to the finer level

$$n_{\text{ts}} = 2^{m-1}, \; m = 4, \; \dots \; , 18. \tag{15}$$

In the same manner, the spatial domain is divided into n_{ex} elements of constant size $\Delta x = 2/n_{\text{ex}}$. The number of elements in spatial direction is given by

$$n_{\text{ex}} = 2^{l-1}, \; l = 4, \; \dots \; , 18. \tag{16}$$

For each simulation, the relative L_2 error e_{lm} at the final time $t_f = 2$ for the spatial refinement level l and temporal refinement level m is evaluated. In practice, we use an element-wise two-point Gaussian quadrature for the spatial integration

$$e_{lm} = \frac{\|(u - u^h)(\cdot, t_f)\|}{\|u(\cdot, t_f)\|} \approx \frac{1}{\|u(\cdot, t_f)\|} \sqrt{\frac{\Delta x}{2} \sum_{e=1}^{n_{\text{ex}}} \sum_{iq=1}^{2} \left(u(x_{iq}^e, t_f) - u^h(x_{iq}^e, t_f) \right)^2}. \tag{17}$$

Additionally, we measure the nodal errors as

$$E_{lm} := \frac{1}{\|u(\cdot, t_f)\|} \sqrt{\Delta x \sum_{i=1}^{n_{\text{ex}}} \left(u(x_i, t_f) - u^h(x_i, t_f) \right)^2}, \tag{18}$$

with the index i running over all nodes, except for the last one. In model problem IBVP 1, node 1 and node $n_{\text{ex}} + 1$ have identical solution values enforced by the periodic boundary conditions. For both model problems, the prefactor with the L_2 norm of the solution at the final time $t_f = 2$ reads

$$\frac{1}{\|u(\cdot, t_f)\|} = e^{2k\pi^2}. \tag{19}$$

Furthermore, we want to remark that the relative L_2 error e_{lm} at the final time is not the only relevant quantity. Conventional a priori error bounds for Galerkin and streamline diffusion discretizations of advection-diffusion problems, as well as estimates for error adaptive mesh refinement are mainly based on the energy norm $\|\nabla(u - u^h)\|$.[21] However, in this section we focus more on the transient nature of the problem and restrict ourselves to the two L_2-error measures (Equations 17 and 18).

To approximate these quantities numerically, simulations are performed for whole-numbered parameter pairs (l, m) corresponding to grid line intersections in Figure 6. Avoiding unnecessary computational cost, we omit combinations of the finest refinement levels as shown in Figure 6. Note that the patch color is based on the mean value of the L_2 error e_{lm} of the four simulations connected by a patch.

To check for spatial convergence, we consider the finest temporal refinement level $m = 18$ and vary $l = 4, \; \dots \; , 12$, which corresponds to the bottom line of the plot in Figure 6. Analogously to investigate temporal convergence, we consider the finest spatial refinement level $l = 18$ and vary $m = 4, \; \dots \; , 12$. This corresponds to the rightmost line of the plot in Figure 6. On the space-time diagonal $l = m$, the numerical values of Δt and Δx coincide. Despite the different units that one would assign to the physical quantities, we use $\Delta t = \Delta x$ to express that the numerical values are equal. Along the curve $\Delta t = \Delta x$, twelve data points $m = l = 4, \; \dots \; , 15$ are generated.

4.1 | Parabolic model problem IBVP 2

In this section, we study the pure diffusion case of the model problem ($a = 0, k = 0.1$)

$$\text{IBVP 2} \quad \begin{cases} \text{res}(u(x,t)) = 0, & x \in]-1, 1[, \quad t \in]0, 2], \\ u(x,t) = \cos(\pi x), & \text{at } t = 0, \\ u(-1,t) = u(1,t) = b(t) = -e^{-k\pi^2 t}, & \text{on } P^D. \end{cases} \tag{20}$$

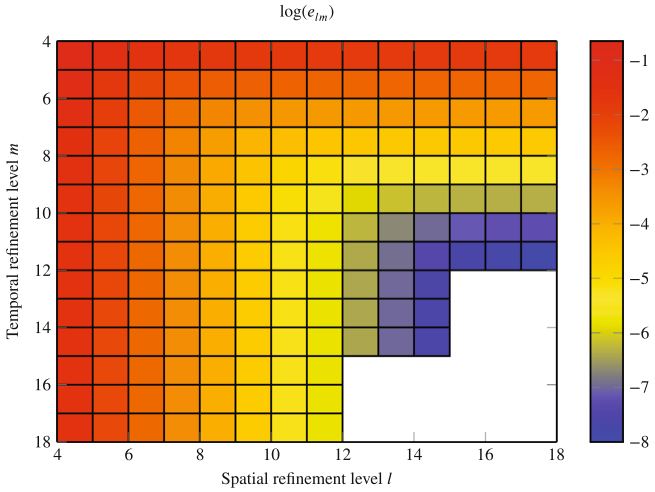

FIGURE 6 Organization of space-time convergence study based on L_2 error e_{lm}.

With the time-dependent Dirichlet boundary conditions $b(t)$, IBVP 2 has the analytical solution

$$u(x,t) = \cos(\pi x)e^{-k\pi^2 t}. \tag{21}$$

The considered advection-diffusion equation (1) thereby reduces to the heat equation. For a corresponding initial boundary value problem with homogeneous boundary conditions, convergence estimates for D-PST discretizations are known from literature. Thomée presents in theorem 12.7 of Reference 41 a superconvergence result for the temporal discretization error at the final time t_f. Considering linear basis functions, the error bound for the parabolic problem can be summarized as

$$\|(u - u^h)(\cdot, t_f)\| \leq C(\Delta t^3 + \Delta x^2), \tag{22}$$

where C is a positive constant independent of Δt and Δx.

In the following, we compare our computational findings to the theoretical result above. The results of the space-time convergence studies are visualized in convergence surfaces (see Figure 7). The surfaces are obtained by plotting the L_2 error e_{lm} in logarithmic scale over the spatial and temporal refinement level indices l and m. Corresponding convergence surfaces based on the nodal error measure can be found in the Appendix A in Figure A2. For both discretization methods, the error plots result in a continuous surface (Figures 7A and A1A). Moreover, the surfaces show, that the error values in the area of the diagonal ($l = m$, $\Delta t = \Delta x$) are influenced by the spatial and temporal mesh size. However, on the finest spatial discretization level ($l = 18$), the error varies only with Δt. The same holds for the finest temporal refinement level ($m = 18$) and Δx. Therefore, extracting the curves $l = 18$ or $m = 18$ from the convergence surfaces gives us the isolated spatial or temporal convergence behavior of the methods.

At first, focusing on the spatial convergence rates shown in Figure 8A, we observe a second-order spatial accuracy for both methods as the curves of D-PST and D-SST coincide. This is to be expected, as the same spatial mesh is used. Moreover, this observation is also in line with the theoretical result given in Equation (22). Next, looking at the temporal convergence rates in Figure 8B, a second-order temporal convergence is observed for both methods. This is in strict contrast to the third-order time accuracy expected from Equation (22).

As pointed out by Voulis and Reusken,[32] the reduced convergence order is due to the time-dependent boundary conditions. Moreover, it is shown in their work that superconvergence can be recovered by applying a temporal interpolation operator to the boundary condition $b(t)$. The use of this discretized boundary condition is equivalent to the time-discontinuous discretization of the boundary condition $\frac{\partial u}{\partial t}(x,t) = \frac{\partial b}{\partial t}(t)$. In our considered test case, the temporal convergence can be improved with the following treatment. On the upper time level $\Omega_u = \Omega(t_u)$ of each space-time slab, the boundary condition is precisely evaluated as

$$u(-1, t_u) = u(1, t_u) = b(t_u) = -e^{-k\pi^2 t_u}. \tag{23}$$

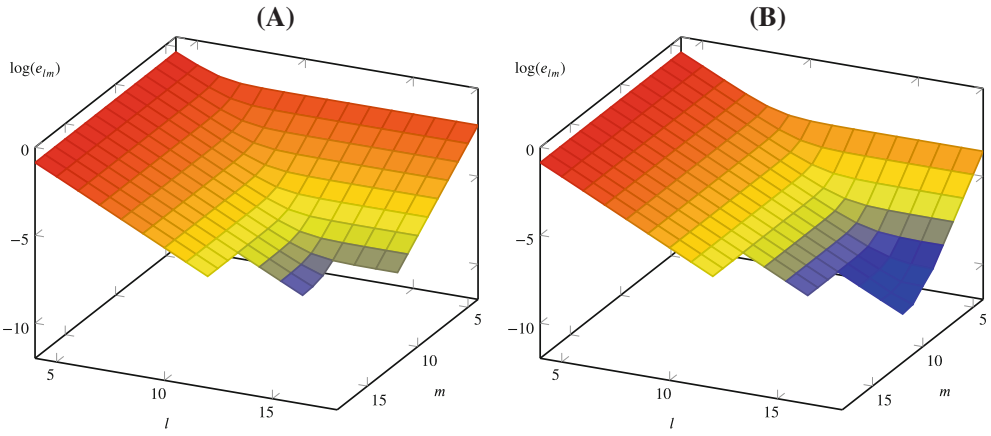

FIGURE 7 Convergence visualization of L_2 error of D-PST discretization of parabolic problem configuration IBVP 2. (A) D-PST; (B) D-PST with $\tilde{b}(t_l)$.

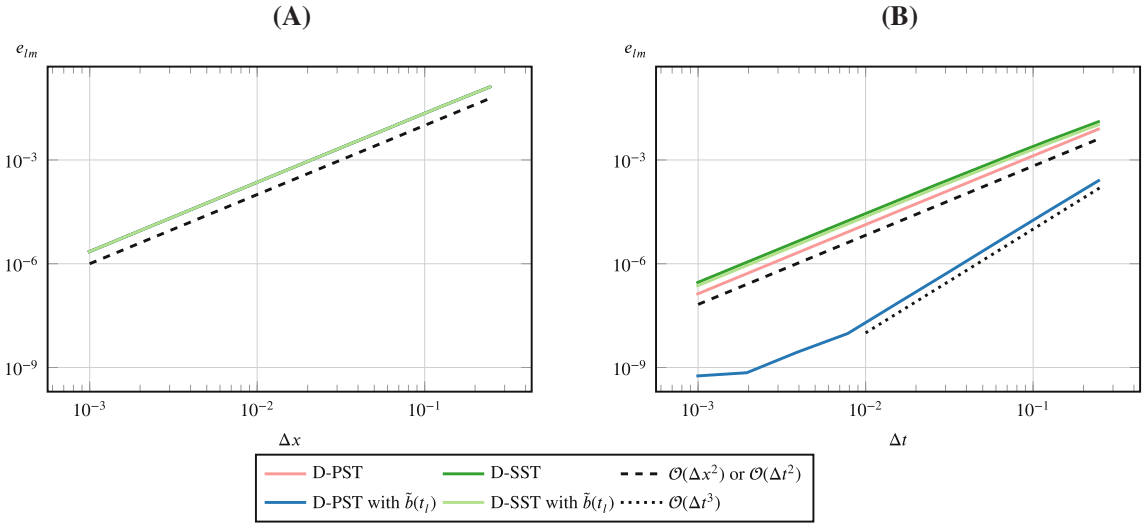

FIGURE 8 Spatial and temporal convergence for IBVP 2. (A) Spatial convergence, $\Delta t = \frac{1}{65{,}536}$; (B) Temporal convergence, $\Delta x = \frac{1}{65{,}536}$.

On the lower time level Ω_l, a modified boundary condition $\tilde{b}(t_l)$ is applied. The modified boundary condition is constructed such that the linear interpolation of the finite element shape functions leads to the correct analytical mean of the boundary condition

$$\frac{1}{2}\left[b(t_u) + \tilde{b}(t_l)\right] \stackrel{!}{=} \frac{1}{\Delta t}\int_{t_l}^{t_u} b(t)dt. \tag{24}$$

For the considered example, this yields

$$\tilde{b}(t_l) = \left[1 + \frac{2}{k\pi^2\Delta t}\left(1 - e^{k\pi^2\Delta t}\right)\right] e^{-k\pi^2 t_u}. \tag{25}$$

Repeating the space-time convergence study with modified boundary conditions, we obtain the results shown in Figures 7B and A1B. Here, D-PST reaches significantly smaller error values in comparison to the case shown in Figure 7A. Returning in the line plots of Figure 8A, it can be seen that the second order spatial convergence of both methods is not affected by the boundary condition treatment as all four curves coincide. But, for D-PST with $\tilde{b}(t_l)$, third-order temporal convergence is indeed obtained (Figure 8B). The result numerically confirms that temporal superconvergence (as stated in Equation 22) can also be obtained for time-dependent boundary conditions with a proper treatment.[32]

For D-SST with $\tilde{b}(t_l)$, only quadratic temporal convergence is observed. The lower convergence order of the D-SST method with treatment of the time-dependent boundary conditions hints at the fact that superconvergence of the D-PST method is linked to the tensor-product structure of the discretization. However, also in case of the D-SST discretization, the proposed treatment of time-dependent boundary conditions is helpful—the error values decrease by approximately 25%.

The purely spatial or temporal refinements are interesting as they show an isolated spatial or temporal convergence behavior, but they are certainly not efficient in terms of computational cost that is required to obtain a certain level of accuracy. Elaborating on this, we assume that the computational cost of a simulation is related to the number of degrees of freedom n_{dof}. For the considered discretizations, n_{dof} can be expressed by the number of time steps n_{ts} and the number or elements in x-direction n_{ex} as

$$n_{\text{dof}} = 2 \cdot n_{\text{ts}} \cdot (n_{\text{ex}} - 1)\,. \tag{26}$$

Since we estimate the total computational cost by the number of degrees of freedom, it is of the order $\mathcal{O}(\frac{1}{\Delta x}\frac{1}{\Delta t})$. This can be used to balance the spatial and temporal discretization to minimize the computational cost for a desired error. The optimal relation between the spatial mesh size and the temporal therefore depends on the relation between the spatial and the temporal convergence order. If the spatial and temporal convergence order match, then the choice $\Delta x = \Delta t$ is optimal. However, if we consider the setting in Equation (22), then the optimal choice is $\Delta x^2 = \Delta t^3$.

In the visualizations of the convergence studies, for example, in Figure 7, we can identify the best space-time refinement strategy as the steepest decent in the convergence surfaces. In Figure 7A, an advantageous space-time refinement strategy for D-SST essentially follows $\Delta t = 4 \cdot \Delta x$. In contrast, for D-PST with $\tilde{b}(t_l)$ (Figure 7B), the second-order spatial accuracy and third-order temporal accuracy lead to an advantageous space-time refinement strategy along the curve $\Delta t^3 = \Delta t^2$.

The L_2 errors along the curves $\Delta t = 4 \cdot \Delta x$ and $\Delta t^3 = \Delta x^2$ are extracted from the convergence surfaces and plotted in Figure 9. On the space-time diagonal with offset ($\Delta t = 4 \cdot \Delta x$, Figure 9A), both methods show a second-order convergence for the computations with and without $\tilde{b}(t_l)$. For D-PST with $\tilde{b}(t_l)$, the curve is in a region where the spatial error dominates, hence, we expect second-order convergence also for this method. However, in contrast to Figure 8A, the curves do not coincide and the treatment of the time-dependent boundary conditions proves advantageous in terms of the absolute error values. Note that transitioning from one data point to the next along the space-time diagonal doubles n_{ts} and n_{ex}.

Following the advantageous refinement strategy for D-PST with $\tilde{b}(t_l)$, Figure 9B shows that the third-order temporal accuracy of D-PST with $\tilde{b}(t_l)$ is retained along the curve $\Delta t^3 = \Delta x^2$. Summarizing the parabolic model problem analysis, both methods, D-PST and D-SST, converge at least quadratically against the analytical solution. With proper treatment, D-PST converges cubically with respect to Δt even for time-dependent boundary conditions.

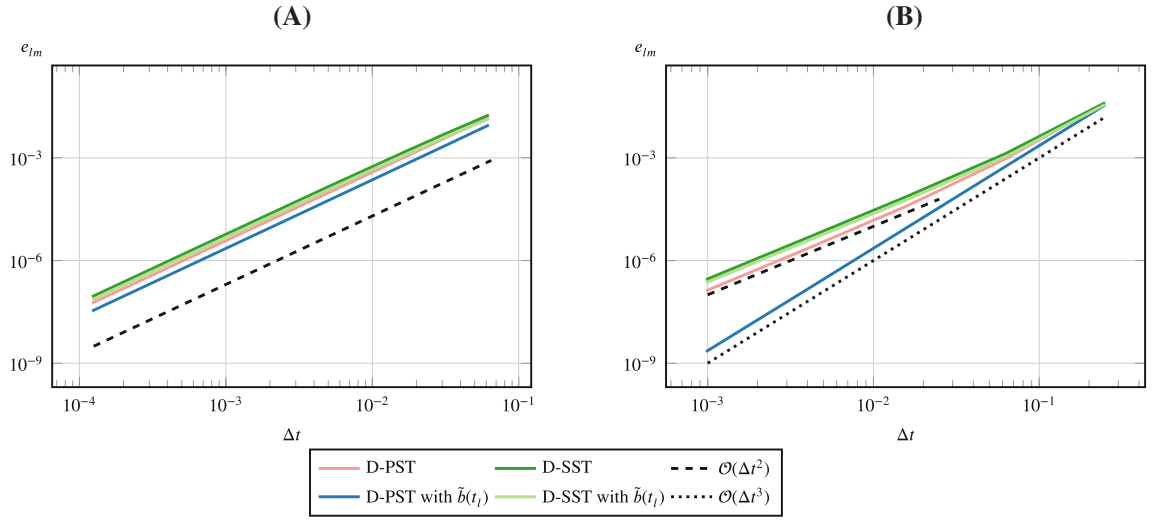

FIGURE 9 Influence of $\tilde{b}(t_l)$ on space-time convergence for IBVP 2. (A) Refinement along $\Delta t = 4 \cdot \Delta x$. (B) Refinement along $\Delta t^3 = \Delta x^2$

4.2 | Advective-diffusive model problem IBVP 1

While the main challenge in the previous Section 4.1 was the treatment of time-dependent boundary conditions, this section investigates the convergence behavior of the methods as the model parameters transition from the parabolic case to advection-diffusion cases and to the hyperbolic case. The numerical error analysis of D-PST and D-SST is therefore continued with the model problem IBVP 1 (Equation 13). Six parameter sets are considered. They include the parabolic case $a = 0$, $k = 0.1$, $\mathrm{Pe} = 0$, next to four advection-diffusion cases with decreasing viscosity $a = 1$, $k = 0.1, 0.01, 0.001, 0.0001$, $\mathrm{Pe} = 1, 10, 100, 1000$ and the hyperbolic case $a = 1$, $k = 0$, $\mathrm{Pe} = \infty$. The periodic boundary conditions do not require the treatment of time-dependent boundary conditions.

As before, the results of the space-time convergence studies are visualized in convergence surfaces. Four representative convergence surfaces are shown in Figure 10. The complete set of twelve surfaces can be found in Figure A3. For all parameter sets, a continuous surface is obtained. Furthermore, for both space-time discretizations, the advection-diffusion cases with increasing Péclet number present a smooth transition from the pure diffusion to the pure advection case. Comparing the parabolic cases (Figure 10A,B), the convergence surfaces of D-PST and D-SST clearly differ. D-PST reaches smaller error values due to the superconvergence of the discretization with tensor-product elements (Equation 22). The hyperbolic cases (Figure 10C,D) show only a slight difference for the simulations on coarse meshes with $\Delta x = \Delta t$, yet, on the finer meshes D-PST and D-SST arrive at very similar results.

After this brief view on the convergence surfaces, we now analyze spatial and temporal convergence by means of line plots. Spatial convergence results are presented in Figure A4. Both space-time methods converge quadratically with respect to Δx for the complete model parameter range from $\mathrm{Pe} = 0$ up to $\mathrm{Pe} = \infty$ and for all values of Δx. Besides the constant convergence rates, there is an influence of the Péclet number on the actual relative error values. The solutions for the more diffusive cases, are slightly more accurate.

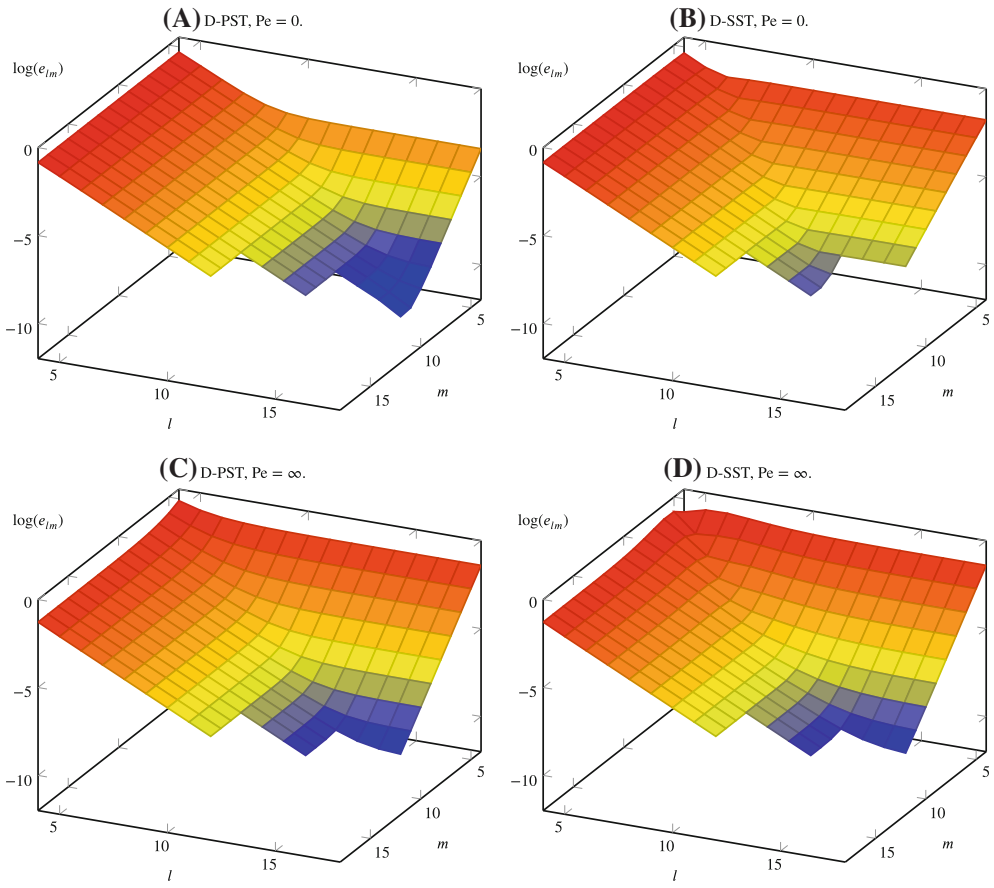

FIGURE 10 Convergence visualization of L_2 error for model problem IBVP 1. (A) D-PST, $\mathrm{Pe} = 0$; (B) D-SST, $\mathrm{Pe} = 0$; (C) D-PST, $\mathrm{Pe} = \infty$; (D) D-SST, $\mathrm{Pe} = \infty$.

Figure 11 collects the results of the temporal convergence study. For this model problem, D-PST is observed to converge cubically with respect to the time step for the complete range of Péclet numbers, despite the fact that the curve of Pe = 0 is shifted to smaller error values as shown in Figure 11A. This behavior is in line with the results obtained by Shakib and Hughes in a Fourier analysis of the purely advective and purely diffusive limiting case of this model problem.[22] Note that the specific mesh connectivity (stencil) of the D-PST discretization is used in the Fourier analysis and the results hence do not apply to a D-SST discretization. The D-SST results presented in Figure 11B show a strong influence of the Péclet number. The method is second-order time accurate in the parabolic case and third-order accurate in the hyperbolic case. For advection-diffusion cases, we observe a smooth transition of the convergence behavior from second to third order. However, rather than converging at a constant intermediate rate, D-SST converges for the advection-diffusion cases cubically up to some $\Delta t_{\text{turn}}(\text{Pe})$, where the convergence rate transitions to two. For smaller Péclet numbers, the transition occurs at larger time steps, which is earlier in the convergence history.

So far, we discussed the convergence of the L_2 errors, but, also the convergence surfaces of the nodal error measure (Equation 18) show interesting features of the discretization methods. The complete set of the 12 nodal error-based convergence surfaces can be found in Figure A5 in the Appendix A. The results of the hyperbolic case are presented in Figure 12. The nodal error visualization of the D-PST results (Figure 12A) is a continuous surface as for the L_2 error. In contrast, the D-SST results (Figure 12B) show a strong discontinuity for the simulations with $\Delta t = \Delta x$. For these cases, the space-time finite element edges align with the characteristic curves along which the solution is transported. We observe that the finite element approximation coincides with the exact solution at the nodes (up to a round off error $\epsilon < 1.0 \times 10^{-10}$) for all refinement levels. This astonishing behavior is described by Demkowicz and Oden as "extra superconvergence."[42] Away from the diagonal $l = m$, error values are obtained that are similar to the ones of D-PST.

Spatial convergence results of the D-PST method in nodal error measure are extracted as line plots and shown in Figure 13A. We see once more a strong influence of the Péclet number on the convergence behavior. In the pure advection case, the method converges in the nodal error measure with fourth order up to a $\Delta x_{\text{turn}}(\text{Pe})$ and then transitions to second order. For smaller Péclet numbers, the transition occurs at larger Δx, that is, earlier in the convergence history. In the simulations with the fourth-order convergence relative to each other, the element size in time direction Δt is very small compared to Δx. In consequence, the small Δt leads to such a small stabilization parameter τ_{SUPG} (Equation 7), that the influence of the SUPG term vanishes and the Galerkin method is recovered. The nodal error of the Galerkin method for the pure advection case is fourth-order accurate with respect to Δx, as shown in the Fourier analysis of Shakib and Hughes.[22] In the pure diffusion case, the method is second-order accurate with respect to Δx over the entire element size range.

Figure 13B shows nodal error results of the D-SST method for the six model parameter sets along the space-time diagonal $\Delta t = \Delta x$. Most notable is the "extra superconvergence" of the SST method with characteristics aligned element edges for the pure advection case. For the five other model parameter sets, we observe a second order space-time convergence along the diagonal $\Delta t = \Delta x$. The curves of the cases with Pe = 0 and Pe = 1 essentially coincide, while the other cases show smaller error values for higher Péclet numbers.

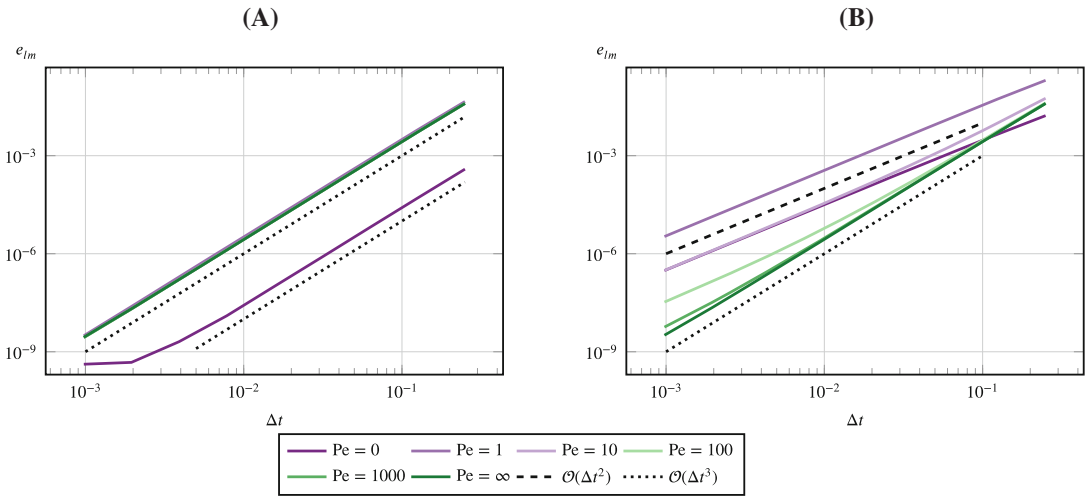

FIGURE 11 Temporal convergence for IBVP 1 for six model parameter sets. (A) D-PST, $\Delta x = \frac{1}{65{,}536}$; (B) D-SST, $\Delta x = \frac{1}{65{,}536}$.

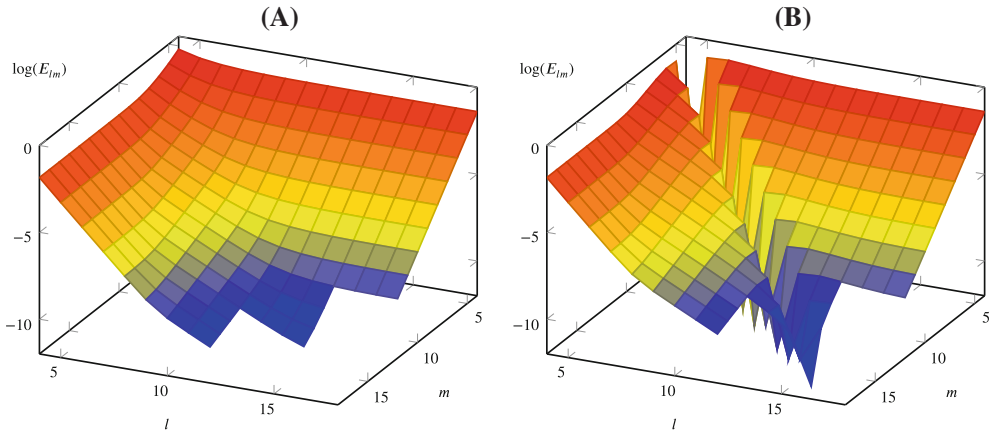

FIGURE 12 Convergence visualization of nodal error measure for IBVP 1 with Pe = ∞. (A) D-PST; (B) D-SST.

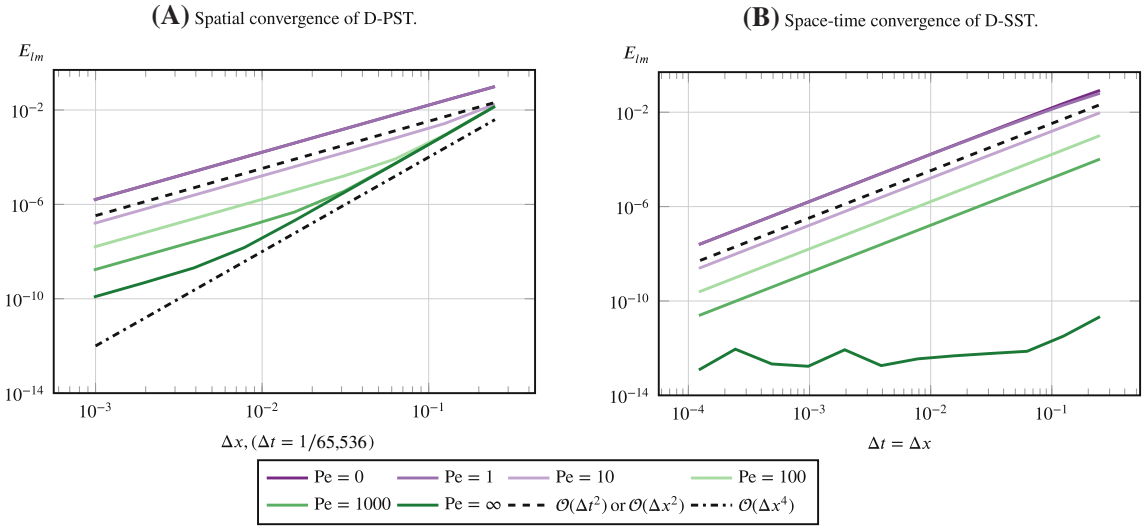

FIGURE 13 Convergence in nodal error measure for IBVP 1 for six parameter sets. (A) Spatial convergence of D-PST; (B) Space-time convergence of D-SST.

Unfortunately, it is highly unlikely that the finite element edges of higher-dimensional space-time meshes are aligned with the solution characteristics for general flow conditions. Therefore, we come to the following outlook for problems of engineering interest. Under the assumption that our findings carry over from the scalar 1D advection-diffusion cases to higher-dimensional cases modeled with (in)compressible Navier–Stokes equations, we expect a spatial accuracy of second order and a temporal accuracy between second and third order. As we have seen, the temporal accuracy of the time-discontinuous space-time methods tends towards third-order depending on how advection-dominated the test case is, on the element type used for discretization, and on the time-(in)dependence and treatment of the boundary conditions.

5 | APPLICATION EXAMPLES

The time-discontinuous space-time discretizations (D-PST and D-SST) have several advantages, for example, with tensor-product elements superconvergence of the L_2-error at the final time can be achieved. However, in practice superconvergence is hard to obtain as it is contingent on several factors, for example, the treatment of time-dependent boundary conditions. Therefore, we use in this section the more flexible time-continuous simplex space-time discretization (C-SST).

5.1 | Piston ring test case

The purpose of the following test case is to demonstrate the capability of time-continuous simplex space-time discretizations (C-SST) to account for complex changes of the spatial computational domain. In this particular simulation, the connectivity of the spatial domain changes multiple times. The boundary conforming tetrahedral space-time mesh is shown in Figure 14.

As a motivational example, we consider the piston ring pack on an internal combustion engine. The piston rings are employed to seal the high-pressure gas in the combustion chamber (i), to prevent engine oil from leaking into the combustion chamber (ii), and to dissipate heat from the piston to the surrounding cylinder to prevent overheating of the piston (iii). In this test case, we investigate the heat flux in a simplified model of a piston ring pack.

Figure 15 shows the two-dimensional geometry of a schematic piston ring pack with only one ring. The considered geometry includes a part of the piston around the groove in which the piston ring is located, as well as a part of the cylinder liner which comes into contact with the piston ring. As shown in Figure 15, the piston ring is represented by a square with a generic side length of 0.5; its corners are rounded with radius $r = 0.1$.

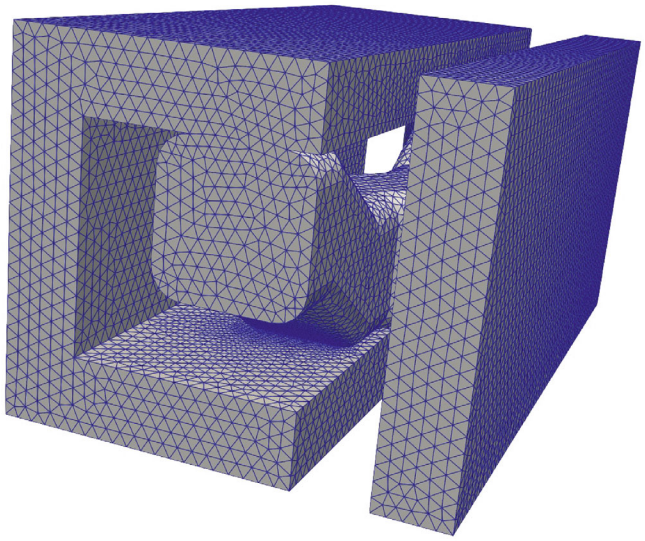

FIGURE 14 Tetrahedral space-time mesh.

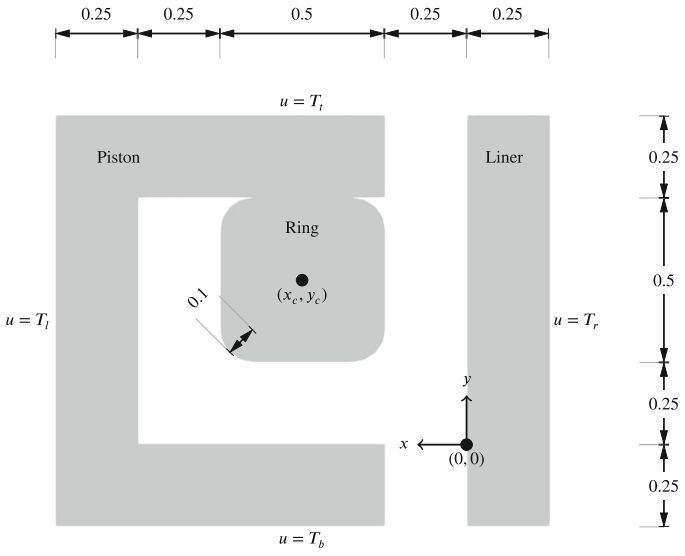

FIGURE 15 Setup of piston ring test case.

In the following simulation, we investigate the conductive heat transfer in the metal parts and across the contact interfaces between piston, ring, and liner. The heat transfer is modeled with the parabolic case of Equation (1), that is, the advection velocity is set to zero and we obtain a Péclet number of zero. The thermal diffusivity in the solids $k = \frac{\kappa}{\rho c_p}$, that accounts for the thermal conductivity κ, density ρ, and specific heat c_p, is here modeled with a generic diffusion coefficient $k = 0.495$, as employed in Equation (1). The test case is further characterized by the temperatures

$$T_t = 423.15, \quad T_b = 403.15, \quad T_l = 403.15 + 20 \cdot \frac{y + 0.25}{1.25}, \quad \text{and } T_r = 373.15, \tag{27}$$

prescribed as Dirichlet boundary conditions on the edges as indicated in Figure 15. On all remaining boundaries, homogeneous Neumann boundary conditions are assumed. The initial boundary value problem on a two-dimensional spatial domain ($n_{\text{sd}} = 2$) is completed with the initial condition

$$u(x, y, t = 0) = T_0 = 373.15 + h(x - 0.01) \cdot \left(30 + 20 \cdot \frac{y + 0.25}{1.25}\right), \tag{28}$$

where $h(x)$ denotes the Heaviside function.

What makes this test case challenging is the ring motion. In the course of an engine working cycle, the piston ring is in contact with different parts of the piston and the liner. We consider a prescribed ring motion defined by the ring center position, $(x_c(t), y_c(t))$, as shown in Figure 16. During the simulated time interval $t \in (0, 2.6)$, the ring is first in contact with the upper edge of the piston groove, then moves downwards and is free-floating for $t \in (0.2, 0.6)$, before it comes into contact with the lower edge of the piston groove. These three states are also visualized in the first three figures in the left column of Figure 17. In the following, the ring moves towards the liner, slides upwards along the liner and finally returns to the initial position.

In a C-SST approach,[9] the given ring motion is included in the computational space-time domain as shown in Figure 14. We used GMSH[43] to discretize the domain with a fully unstructured space-time mesh. Moreover, the mesh is refined in areas where large spatial and temporal solution gradient are expected, that is, the curves where the ring comes into contact with the piston and the liner in the course of the simulation. The resulting (coarse) mesh consists of 151,911 tetrahedral elements connecting 35,341 nodes. In addition to the coarse discretization (Figure 14), a fine mesh with 1,431,696 elements and 274,464 nodes is generated so that the convergence can be verified. The solution to the resulting linear equation system is iteratively approximated with an ILUT($50, 1 \times 10^{-4}$)-preconditioned parallel FGMRES solver.[44-46] With a Krylov-space dimension of 20 in the GMRES method, the relative residual $\|\mathbf{Ax} - \mathbf{b}\|/\|\mathbf{b}\|$ drops below 1×1^{-13} with three restarts.

The simulation results are collected in Figures 17 and 18. Figure 17 shows the temperature distribution in the piston ring pack at eight time instances. Most of the time, the temperature solution in the piston and liner parts closely follows the prescribed boundary conditions. Larger spatial temperature variations are primarily encountered in ring. In particular at $t = 2.0$, the ring directly connects the hot upper groove edge of the piston with the cooler liner. As indicated by the large temperature gradients, this configuration leads to the maximal conductive heat transfer.

In Figure 18, the temperature at the piston ring center, $T(x_c(t), y_c(t))$, is plotted over time. It is observed that the temperature is approximately constant during the interval $t \in (0.2, 0.6)$, which is expected as there is no conductive heat transfer

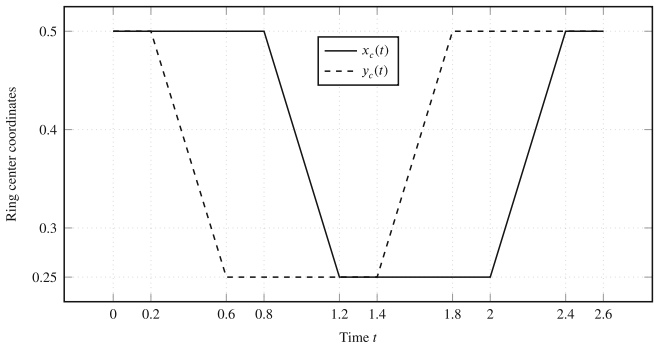

FIGURE 16 Ring motion.

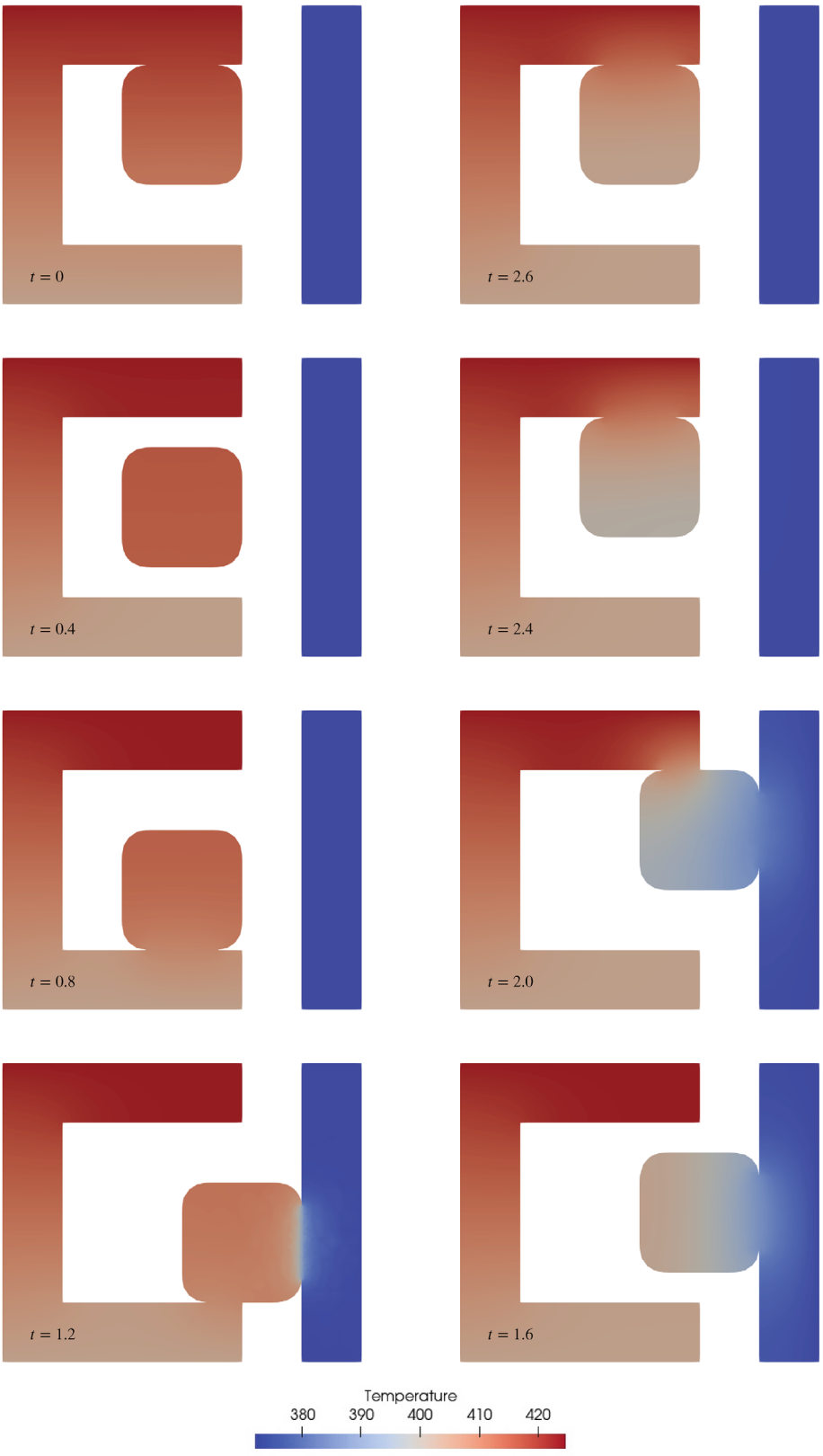

FIGURE 17 Temporal evolution of temperature in piston ring pack.

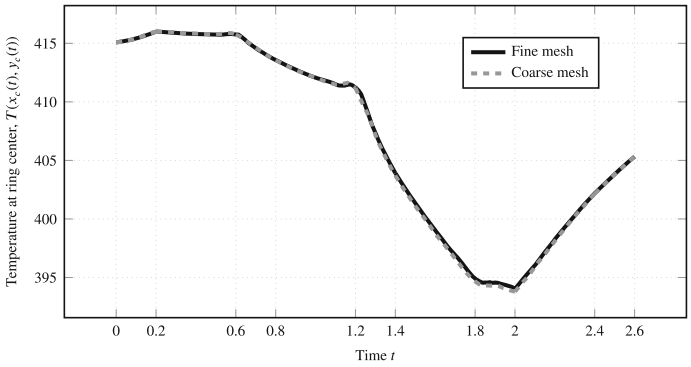

FIGURE 18 Temperature evolution at ring center.

to or from the free-floating ring. The strongest decrease in temperature is observed during the interval $t \in (1.2, 1.4)$, when the ring first comes into contact with the cooler liner. The minimal temperature value is reached at $t = 2.0$, before the ring again detaches from the liner and is heated from the upper edge of the piston groove. Moreover, the comparison of the temperature evolution computed on the coarse mesh and the fine mesh (Figure 18) indicates that the coarse mesh resolution is sufficient to provide an acceptable accuracy.

5.2 | Subtractive manufacturing test case

The geometry of this three-dimensional transient heat flux simulation is based on a rectangular cuboid (Figure 19) with the edge lengths $l_x = 2, l_y = 1$, and $l_z = 0.5$. The origin of the spatial coordinate system is located at the center of the bottom face of the cuboid such that $x \in [-1, 1], y \in [-0.5, 0.5], z \in [0, 0.5]$. Over a time interval with $t \in [0, 2]$, a cylindrical tool with radius $r = 0.25$, removes material and eventually splits the block with a straight cut at an angle of 30 degree toward the perpendicular. The two resulting pieces are rotational symmetric around $(x = 0, y = 0)$.

Material properties are chosen to be identical with the piston ring test case (Section 5.1). Moreover, the IBVP is characterized by the temperatures

$$T_l = 293.15, \qquad T_r = 303.15, \qquad \text{and} \qquad T_t = 343.15 + 80 \cdot z, \tag{29}$$

prescribed as Dirichlet boundary conditions on the faces $x = -1$, $x = 1$, and the tool face, respectively. Homogeneous Neumann boundary conditions are assumed on all remaining boundaries. As initial condition, a linear interpolation between the wall temperatures is prescribed, namely $T_0 = 293.15 + 5 \cdot (x + 1.0)$.

To solve the three-dimensional transient problem with a C-SST approach, a four-dimensional mesh is required. The specific test case allows for a pentatope mesh generation based on a plane extrusion of a tetrahedral mesh.[8] The resulting mesh consists of 7,869,160 pentatope elements and has 391,754 nodes. Spatial and temporal element sizes correspond to the coarse mesh resolution in Section 5.1, which was found to provide acceptable accuracy (Figure 18). Please, note that also pentatope meshes for more complex geometries can be created with an additional elastic mesh update.[9] Detailed descriptions of the simulation workflow with four-dimensional meshes are provided in our previous publications.[8,9,15] Furthermore, the approach to solve the linear equation system is the same as for the three-dimensional mesh (Section 5.1). With a moderate increase of the Krylov-space dimension in the GMRES method to 50, the relative residual $\|\mathbf{Ax} - \mathbf{b}\|/\|\mathbf{b}\|$ drops below 1×10^{-11} with four restarts.

The results of the simulation are presented in Figures 19 and 20. The temperature distribution in the workpiece is shown for six time instance during the subtractive manufacturing process (Figure 19). The hot face of the tool clearly acts as a heat source where it is in contact with the workpiece. At $t = 0.4$, a three-dimensional temperature distribution in the workpiece can be observed. It is caused by the tool temperature T_t that varies with the z-coordinate. Once the tool has passed, for example, at $t = 1.0$ for $x = -0.6, y = -0.5$, the workpiece is again cooled from the two sides with fixed temperatures, T_l and T_r. To allow for a more quantitative comparison, Figure 20 shows the temperature evolution at two fixed positions in the workpiece $(x = \pm 0.5, y = 0, z = 0.25)$. Due to the skew cut, the temperature at the left $(x = -0.5)$

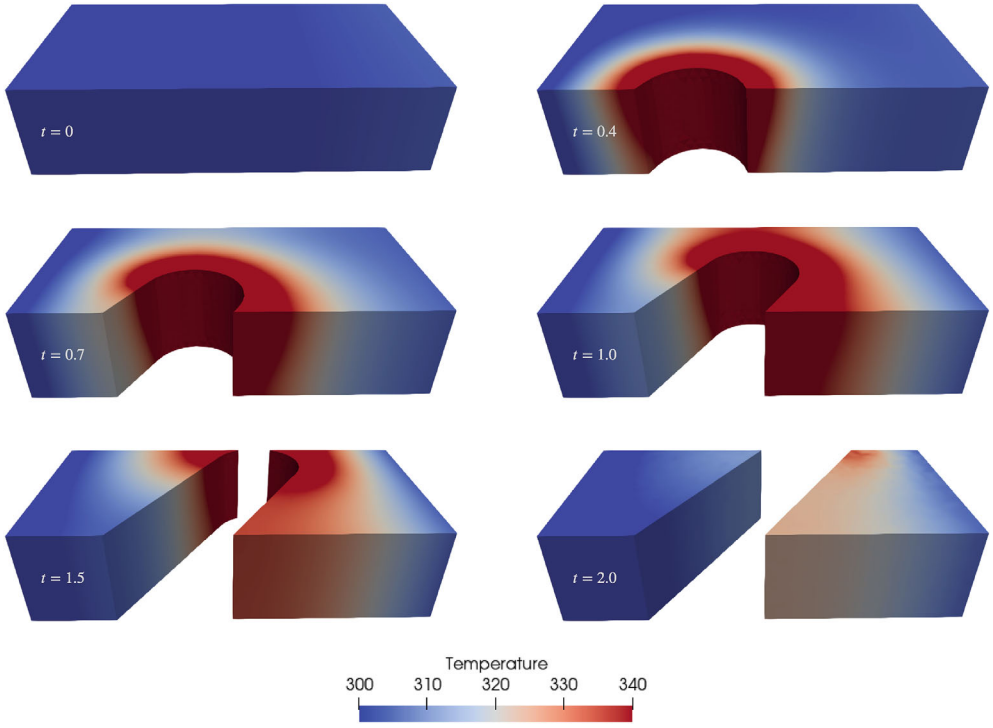

FIGURE 19 Workpiece temperature distribution during subtractive manufacturing process.

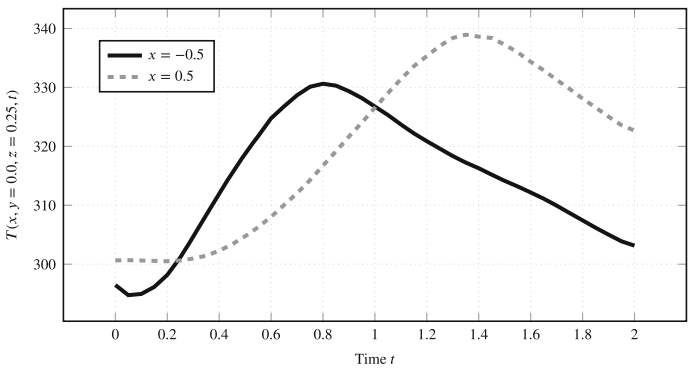

FIGURE 20 Point-wise temperature evolution during subtractive manufacturing process.

increases first. Moreover, the temperature evolution at $x = 0.5$ reaches a higher maximum value, which is reasonable given the wall temperatures $T_r > T_l$.

In summary, the obtained results confirm that C-SST discretizations can also easily handle three-dimensional spatial computational domains undergoing complex changes.

6 | CONCLUSIONS

In this paper, we described four space-time finite element methods that result from the combination of tensor-product and simplex-type elements with globally continuous interpolations of the spatial domain and a continuous or discontinuous interpolation in temporal direction. Descriptive naming was proposed, and all four methods were successfully applied to an advection-diffusion model problem. Theoretical background and a detailed numerical convergence analysis were presented for the time-discontinuous space-time methods (D-PST and D-SST). Based on the L_2-error at the final time, it was observed that the temporal accuracy of the methods tends toward third order. For a parabolic model problem, the

influence of time-dependent boundary conditions, their treatment, and the element type (prismatic or simplex) of the discretization was studied. For a second model problem with analytical solution, the influence of the element type and the Péclet number on the convergence behavior was precisely characterized. Throughout the tests and for all four methods, a spatial accuracy of second order and a temporal accuracy between second and third order was observed.

Which method to chose depends on the requirements of a specific application case. While the C-PST method was included mostly for sake of completeness, a D-PST discretization is probably the method of choice when a constant time-step size in the entire domain fits the application case. Cases that require local temporal refinement, can benefit from a D-SST discretization (Figure 2A). Lastly, when complex changes of the spatial computational domain occur, a C-SST discretization can achieve a boundary-conforming space-time mesh as demonstrated in Section 5, where we used the C-SST method in challenging heat transfer simulations of a piston-ring geometry and a subtractive manufacturing process.

ACKNOWLEDGMENTS

The authors gratefully acknowledge the computing time granted by the JARA Vergabegremium and provided on the JARA Partition part of the supercomputer CLAIX at RWTH Aachen University. Max von Danwitz gratefully acknowledges the funding by *dtec.bw*—Digitalization and Technology Research Center of the Bundeswehr under the project *RISK.twin*. *dtec.bw* is funded by the European Union – NextGenerationEU. Open Access funding enabled and organized by Projekt DEAL.

DATA AVAILABILITY STATEMENT

The data that support the findings of this study are available from the corresponding author upon reasonable request.

ORCID

Max von Danwitz https://orcid.org/0000-0002-2814-0027
Norbert Hosters https://orcid.org/0000-0003-1174-4446
Marek Behr https://orcid.org/0000-0003-4257-8276

REFERENCES

1. Hughes TJ, Hulbert GM. Space-time finite element methods for elastodynamics: formulations and error estimates. *Comput Methods Appl Mech Eng*. 1988;66(3):339-363. doi:10.1016/0045-7825(88)90006-0
2. Langer U, Neumüller M, Schafelner A. Space-time finite element methods for parabolic evolution problems with variable coefficients. In: Apel T, Langer U, Meyer A, Steinbach O, eds. *Advanced Finite Element Methods with Applications: Selected Papers from the 30th Chemnitz Finite Element Symposium 2017*. Lecture Notes in Computational Science and Engineering. Springer; 2019:247-275.
3. Sivas AA, Southworth BS, Rhebergen S. AIR algebraic multigrid for a space-time Hybridizable discontinuous Galerkin discretization of advection(-diffusion). *SIAM J Sci Comput*. 2021;43(5):A3393-A3416. doi:10.1137/20M1375103
4. Tezduyar TE, Behr M, Liou J. A new strategy for finite element computations involving moving boundaries and interfaces–the DSD/ST procedure: I. The concept and the preliminary numerical tests. *Comput Methods Appl Mech Eng*. 1992;94(3):339-351.
5. Hübner B, Walhorn E, Dinkler D. A monolithic approach to fluid–structure interaction using space–time finite elements. *Comput Methods Appl Mech Eng*. 2004;193(23–26):2087-2104.
6. Sathe S, Tezduyar TE. Modeling of fluid–structure interactions with the space–time finite elements: contact problems. *Comput Mech*. 2008;43(1):51.
7. Spenke T, Hosters N, Behr M. A multi-vector interface quasi-Newton method with linear complexity for partitioned fluid–structure interaction. *Comput Methods Appl Mech Eng*. 2020;361:112810.
8. Behr M. Simplex space-time meshes in finite element simulations. *Int J Numer Methods Fluids*. 2008;57(9):1421-1434. doi:10.1002/fld.1796
9. von Danwitz M, Antony P, Key F, Hosters N, Behr M. Four-dimensional elastically deformed simplex space-time meshes for domains with time-variant topology. *Int J Numer Methods Fluids*. 2021;93(12):3490-3506. doi:10.1002/fld.5042
10. Karyofylli V, Frings M, Elgeti S, Behr M. Simplex space-time meshes in two-phase flow simulations. *Int J Numer Methods Fluids*. 2018;86:218-230. doi:10.1002/fld.4414
11. Karyofylli V, Wendling L, Make M, Hosters N, Behr M. Simplex space-time meshes in thermally coupled two-phase flow simulations of mold filling. *Comput Fluids*. 2019;192:104261.
12. Gesenhues L, Behr M. Simulating dense granular flow using the μ(I)-rheology within a space-time framework. *Int J Numer Methods Fluids*. 2021;93(9):2889-2904. doi:10.1002/fld.5014
13. Rendall TC, Allen CB, Power ED. Conservative unsteady aerodynamic simulation of arbitrary boundary motion using structured and unstructured meshes in time. *Int J Numer Methods Fluids*. 2012;70(12):1518-1542.
14. Wang L, Persson PO. A high-order discontinuous Galerkin method with unstructured space–time meshes for two-dimensional compressible flows on domains with large deformations. *Comput Fluids*. 2015;118:53-68.
15. von Danwitz M, Karyofylli V, Hosters N, Behr M. Simplex space-time meshes in compressible flow simulations. *Int J Numer Methods Fluids*. 2019; 91:29-48. doi: 10.1002/fld.4743

16. Karabelas E, Neumüller M. Generating admissible space-time meshes for moving domains in (d + 1) dimensions. *Space-Time Methods*. Radon Series on Computational and Applied Mathematics. De Gruyter; 2019:185-206.
17. Boissonnat JD, Kachanovich S, Wintraecken M. Triangulating submanifolds: an elementary and quantified version of Whitney's method. *Discr Comput Geometry*. 2021;66(1):386-434. doi:10.1007/s00454-020-00250-8
18. Caplan PC, Haimes R, Darmofal DL, Galbraith MC. Four-dimensional anisotropic mesh adaptation. *Comput Aid Des*. 2020;129:102915.
19. Takizawa K, Ueda Y, Tezduyar TE. A node-numbering-invariant directional length scale for simplex elements. *Math Models Methods Appl Sci*. 2019;29(14):2719-2753.
20. Frontin CV, Walters GS, Witherden FD, Lee CW, Williams DM, Darmofal DL. Foundations of space-time finite element methods: polytopes, interpolation, and integration. *Appl Numer Math*. 2021;166:92-113. doi:10.1016/j.apnum.2021.03.019
21. Elman HC, Silvester DJ, Wathen AJ. *Finite Elements and Fast Iterative Solvers: with Applications in Incompressible Fluid Dynamics*. 2nd. ed. Oxford University Press; 2014.
22. Shakib F, Hughes TJ. A new finite element formulation for computational fluid dynamics: IX. Fourier analysis of space-time Galerkin/least-squares algorithms. *Comput Methods Appl Mech Eng*. 1991;87(1):35-58. doi:10.1016/0045-7825(91)90145-v
23. Donea J, Huerta A. *Finite Element Methods for Flow Problems*. 1st ed. John Wiley & Sons; 2003.
24. Lozinski A, Picasso M, Prachittham V. An anisotropic error estimator for the crank-Nicolson method: application to a parabolic problem. *Siam J Sci Comput*. 2009;31:2757-2783. doi:10.1137/080715135
25. Dubuis S, Picasso M. An adaptive algorithm for the time dependent transport equation with anisotropic finite elements and the crank–Nicolson scheme. *J Sci Comput*. 2018;75(1):350-375. doi:10.1007/s10915-017-0537-1
26. Hansbo P. A crank–Nicolson type space–time finite element method for computing on moving meshes. *J Comput Phys*. 2000;159(2):274-289. doi:10.1006/jcph.2000.6436
27. Aziz AK, Monk P. Continuous finite elements in space and time for the heat equation. *Math Comput*. 1989;52(186):255-274. doi:10.1090/s0025-5718-1989-0983310-2
28. Steinbach O. Space-time finite element methods for parabolic problems. *Comput Methods Appl Math*. 2015;15(4):551-566. doi:10.1515/cmam-2015-0026
29. Langer U, Schafelner A. Space-time finite element methods for parabolic initial-boundary value problems with non-smooth solutions. Lirkov I, Margenov S In: *International Conference on Large-Scale Scientific Computing*. Springer; 2020: 593-600.
30. Langer U, Schafelner A. Space-time hexahedral finite element methods for parabolic evolution problems. *arXiv:2103.13835*. 2021.
31. Langer U, Zank M. Efficient direct space-time finite element solvers for parabolic initial-boundary value problems in anisotropic Sobolev spaces. *According to the SIAM Journal on Scientific Computing website*. 2021;43(4):A2714-A2736. doi:10.1137/20m1358128
32. Voulis I, Reusken A. Discontinuous Galerkin time discretization methods for parabolic problems with linear constraints. *J Numer Math*. 2019;27(3):155-182. doi:10.1515/jnma-2018-0013
33. Quarteroni A, Sacco R, Saleri F. *Numerical Mathematics*. 2nd. ed. Springer; 2006.
34. Ern A, Guermond JL. *Theory and Practice of Finite Elements*. 1st ed. Springer; 2004.
35. Brooks AN, Hughes TJR. Streamline upwind/Petrov-Galerkin formulations for convection dominated flows with particular emphasis on the incompressible Navier-stokes equations. *Comput Methods Appl Mech Eng*. 1982;32(1–3):199-259.
36. Bazilevs Y, Calo V, Cottrell J, Hughes T, Reali A, Scovazzi G. Variational multiscale residual-based turbulence modeling for large eddy simulation of incompressible flows. *Comput Methods Appl Mech Eng*. 2007;197(1):173-201. doi:10.1016/j.cma.2007.07.016
37. Pauli L, Behr M. On stabilized space-time FEM for anisotropic meshes: incompressible Navier–stokes equations and applications to blood flow in medical devices. *Int J Numer Methods Fluids*. 2017;85:189-209.
38. Knechtges P. *Simulation of Viscoelastic Free-Surface Flows* PhD thesis. RWTH Aachen University. 2018.
39. Jansen KE, Collis SS, Whiting C, Shakib F. A better consistency for low-order stabilized finite element methods. *Comput Methods Appl Mech Eng*. 1999;174(1):153-170. doi:10.1016/s0045-7825(98)00284-9
40. Mojtabi A, Deville MO. One-dimensional linear advection–diffusion equation: analytical and finite element solutions. *Comput Fluids*. 2015;107:189-195. doi:10.1016/j.compfluid.2014.11.006
41. Thomée V. *Galerkin Finite Element Methods for Parabolic Problems*. 2nd ed. Springer; 2006.
42. Demkowicz L, Oden J. An adaptive characteristic Petrov-Galerkin finite element method for convection-dominated linear and nonlinear parabolic problems in one space variable. *J Comput Phys*. 1986;67(1):188-213. doi:10.1016/0021-9991(86)90121-x
43. Geuzaine C, Remacle JF. Gmsh: a 3-D finite element mesh generator with built-in pre-and post-processing facilities. *Int J Numer Methods Eng*. 2009;79(11):1309-1331.
44. Saad Y. A flexible inner-outer preconditioned GMRES algorithm. *SIAM J Sci Comput*. 1993;14(2):461-469.
45. Saad Y. ILUT: a dual threshold incomplete LU factorization. *Numer Linear Algebra Applic*. 1994;1(4):387-402.
46. Behr M, Tezduyar TE. Finite element solution strategies for large-scale flow simulations. *Comput Methods Appl Mech Eng*. 1994;112(1–4):3-24.

How to cite this article: von Danwitz M, Voulis I, Hosters N, Behr M. Time-continuous and time-discontinuous space-time finite elements for advection-diffusion problems. *Int J Numer Methods Eng*. 2023;124(14):3117-3144. doi: 10.1002/nme.7241

APPENDIX A

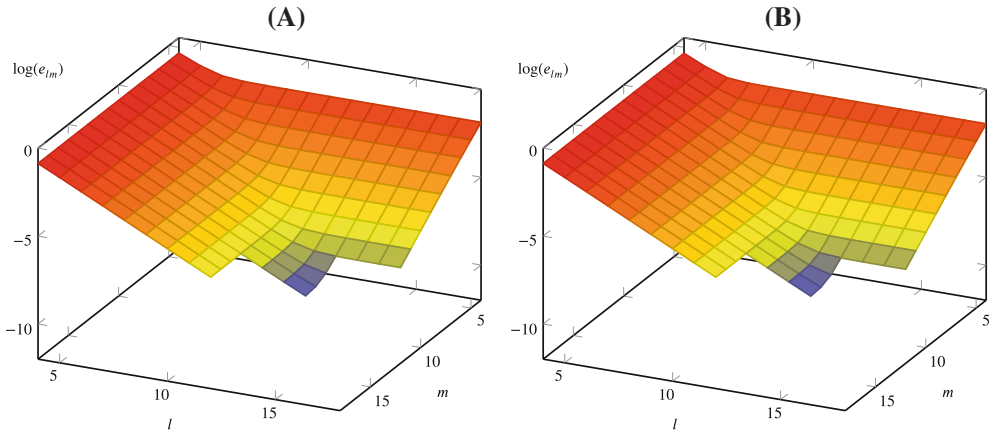

FIGURE A1 Convergence visualization of L_2 error of D-SST discretization of IBVP 2. (A) D-SST; (B) D-SST with $\tilde{b}(t_l)$.

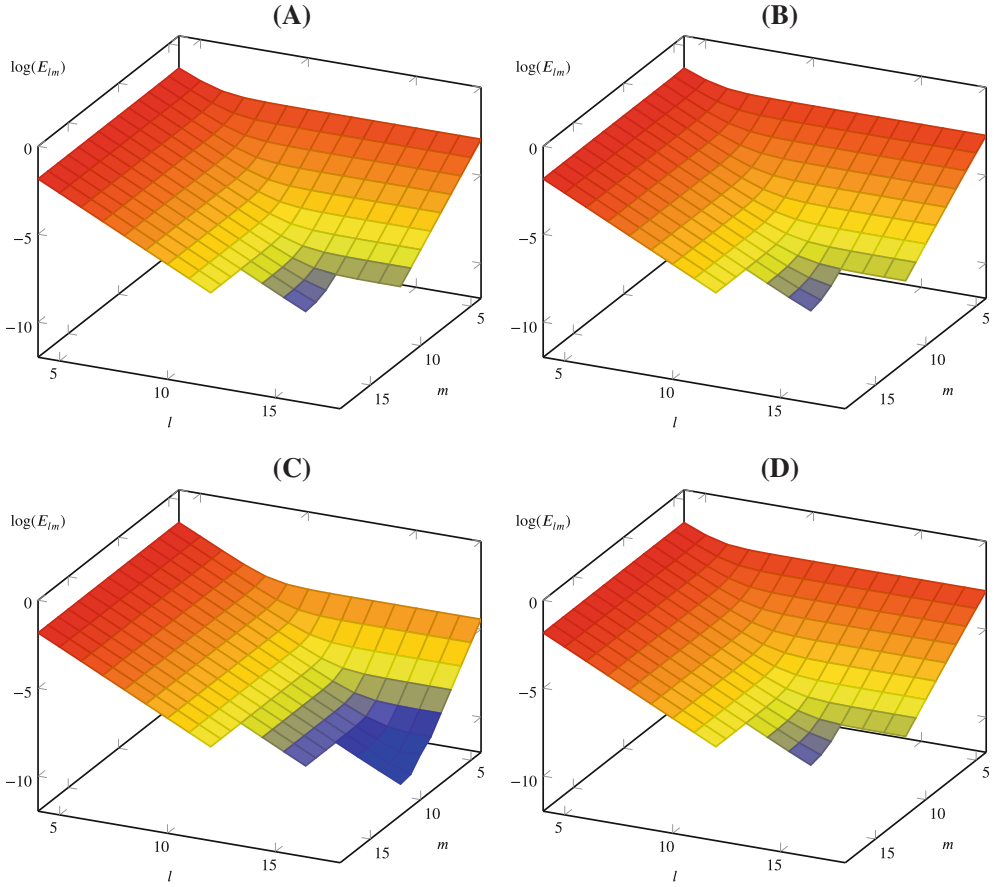

FIGURE A2 Convergence of nodal error measure for parabolic problem IBVP 2. (A) D-PST; (B) D-SST; (C) D-PST with $\tilde{b}(t_l)$; (D) D-SST with $\tilde{b}(t_l)$.

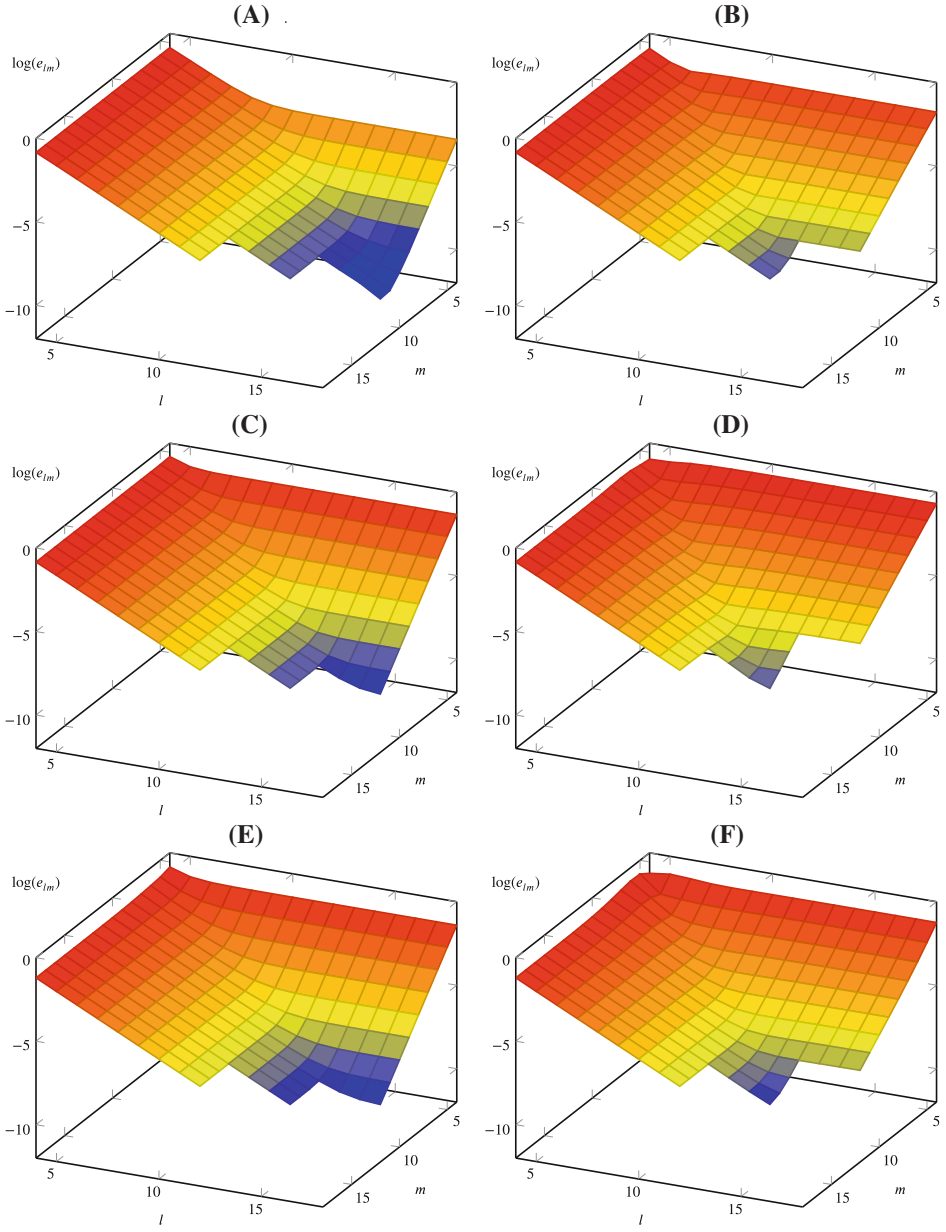

FIGURE A3 Convergence visualization of L_2 error for model problem IBVP 1. (A) D-PST, Pe = 0; (B) D-SST, Pe = 0; (C) D-PST, Pe = 1; (D) D-SST, Pe = 1; (E) D-PST, Pe = 10; (F) D-SST, Pe = 10; (G) D-PST, Pe = 100; (H) D-SST, Pe = 100; (I) D-PST, Pe = 1000; (J) D-SST, Pe = 1000; (K) D-PST, Pe = ∞; (L) D-SST, Pe = ∞.

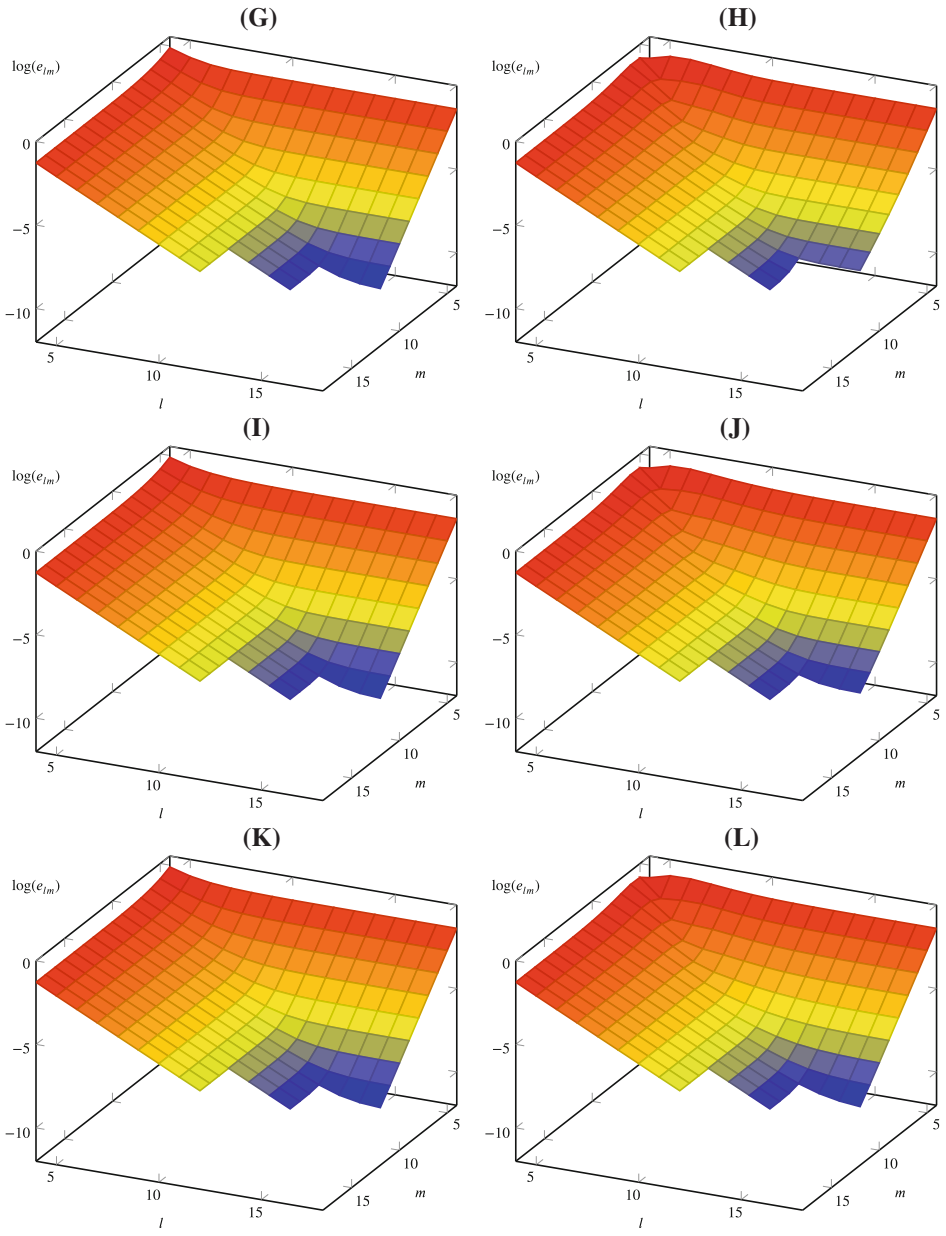

FIGURE A3 (Continued)

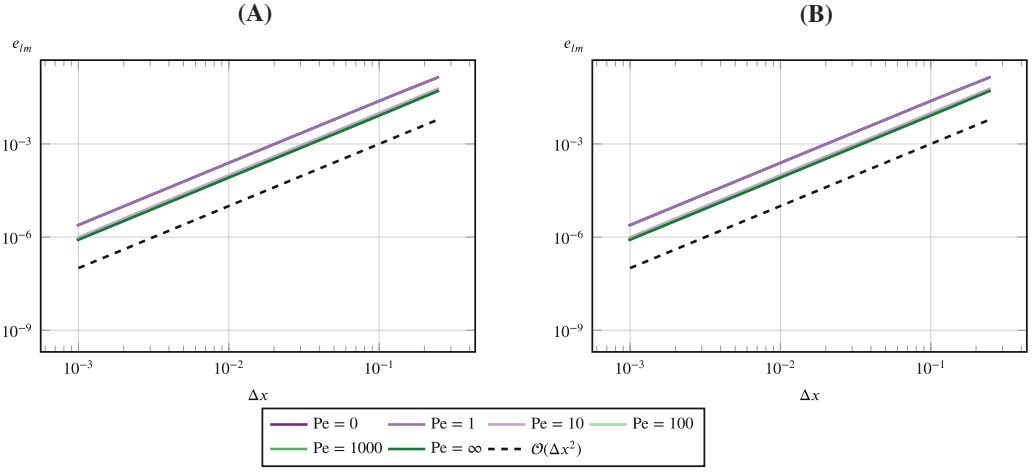

FIGURE A4 Spatial convergence for IBVP 1 for six model parameter sets. (A) D-PST, $\Delta t = \frac{1}{65{,}536}$; (B) D-SST, $\Delta t = \frac{1}{65{,}536}$.

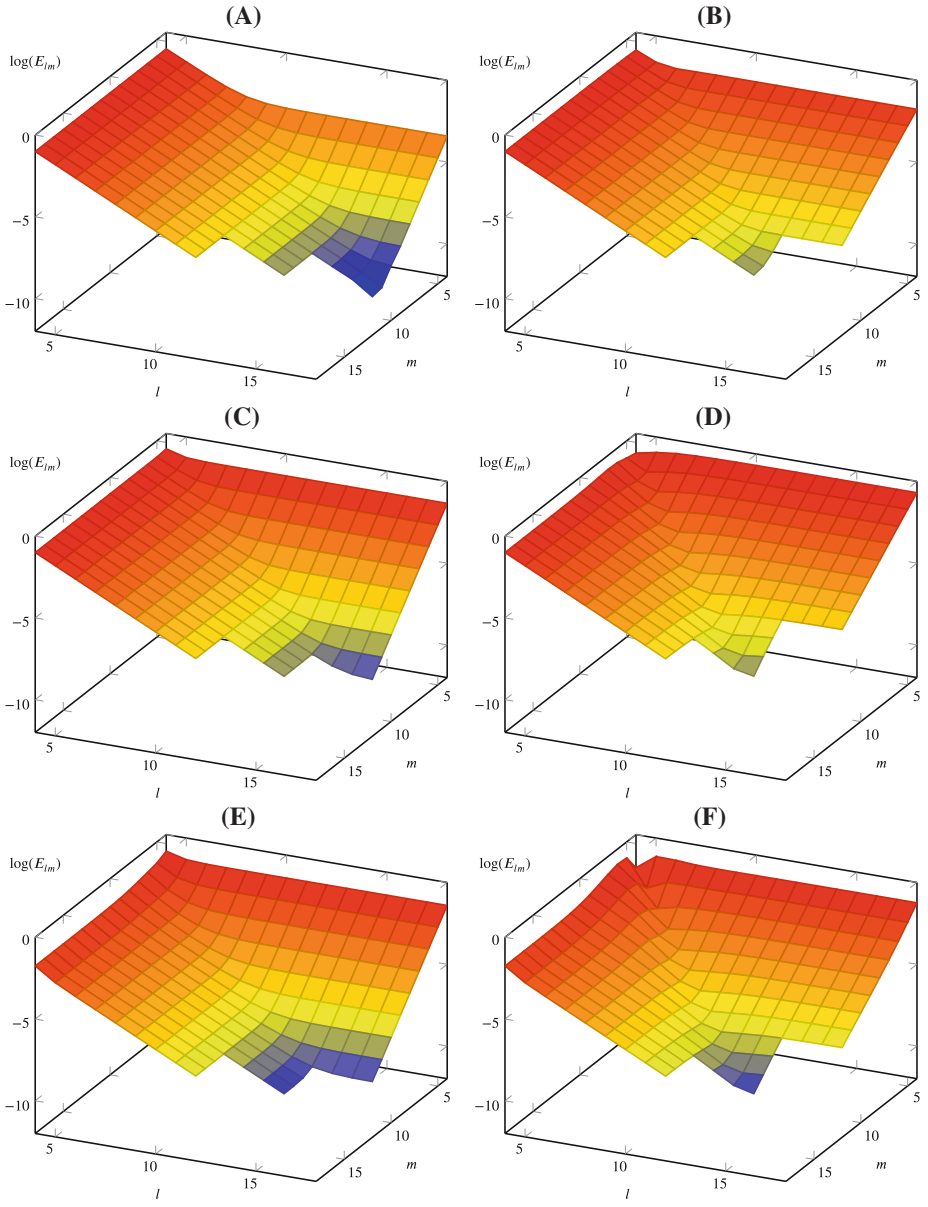

FIGURE A5 Convergence visualization of nodal error for model problem IBVP 1. (A) D-PST, Pe = 0; (B) D-SST, Pe = 0; (C) D-PST, Pe = 1; (D) D-SST, Pe = 1; (E) D-PST, Pe = 10; (F) D-SST, Pe = 10; (G) D-PST, Pe = 100; (H) D-SST, Pe = 100; (I) D-PST, Pe = 1000; (J) D-SST, Pe = 1000; (K) (k) D-PST, Pe = ∞; (L)D-SST, Pe = ∞.

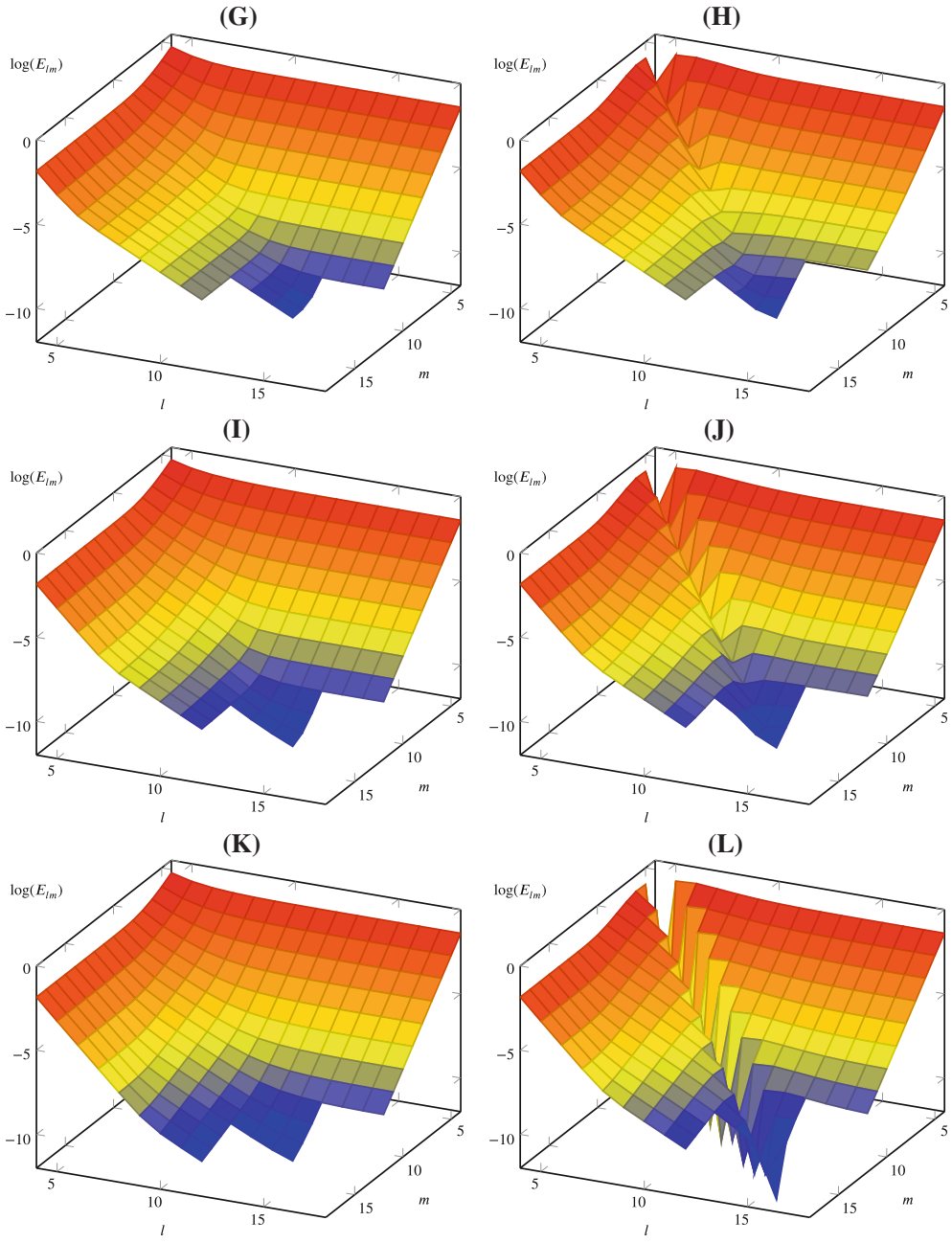

FIGURE A5 (Continued)